



CZECH TECHNICAL UNIVERSITY IN PRAGUE

**Faculty of Civil Engineering
Department of Mechanics**

**Micromechanical Parameter Identification
Using the Bayes Method**

Master's Thesis

Study branch: Konstrukce pozemních staveb

Study program: Stavební inženýrství

Supervisor: prof. Ing. Jan Zeman, Ph.D.

Bc. Liya Gaynutdinova

Prague, 2020



ZADÁNÍ DIPLOMOVÉ PRÁCE

I. OSOBNÍ A STUDIJNÍ ÚDAJE

Příjmení: Gaynutdinova Jméno: Liya Osobní číslo: 458584
Zadávající katedra: Katedra mechaniky
Studijní program: Stavební inženýrství
Studijní obor: Konstrukce pozemních staveb

II. ÚDAJE K DIPLOMOVÉ PRÁCI

Název diplomové práce: Micromechanical Parameter Identification using the Bayes Method

Název diplomové práce anglicky: Micromechanical Parameter Identification using the Bayes Method

Pokyny pro vypracování:

V rámci diplomové práce se studentka seznámí s problematikou výpočetního určení vlastností složek heterogenních materiálů z dat získaných pomocí metod korelace digitálního obrazu (KDO). Vlastní práce pak bude zahrnovat

1. Seznámení se s problematikou KDO [1]
2. Formulace inverzní úlohy a její diskretizace pomocí metody konečných prvků [1,3]
3. Řešení inverzní úlohy s využitím Bayesova přístupu [2]
4. Implementace výsledného algoritmu v MATLABu, otestování algoritmu
5. Studium vlivu aproximace okrajových podmínek [3]

Volitelnou součástí diplomové práce je porovnání výsledků s deterministickými identifikačními metodami představenými v [1].

Seznam doporučené literatury:

- [1] Rokoš, O., Hoefnagels, J. P. M., Peerlings, R. H. J., & Geers, M. G. D. (2018). On micromechanical parameter identification with integrated DIC and the role of accuracy in kinematic boundary conditions. *International Journal of Solids and Structures*, 146, 241-259.
- [2] Rosić, B. V., Kučerová, A., Sýkora, J., Pajonk, O., Litvinenko, A., & Matthies, H. G. (2013). Parameter identification in a probabilistic setting. *Engineering Structures*, 50, 179-196.
- [3] D. Xiu, *Numerical Methods for Stochastic Computations: A Spectral Method Approach*, Princeton University Press, 2010.

Jméno vedoucího diplomové práce: Jan Zeman

Datum zadání diplomové práce: 22.9.2020 Termín odevzdání diplomové práce: 4.1.2021

Údaj uveďte v souladu s datem v časovém plánu příslušného ak. roku


Podpis vedoucího práce


Podpis vedoucího katedry

III. PŘEVZETÍ ZADÁNÍ

Beru na vědomí, že jsem povinen vypracovat diplomovou práci samostatně, bez cizí pomoci, s výjimkou poskytnutých konzultací. Seznam použité literatury, jiných pramenů a jmen konzultantů je nutné uvést v diplomové práci a při citování postupovat v souladu s metodickou příručkou ČVUT „Jak psát vysokoškolské závěrečné práce“ a metodickým pokynem ČVUT „O dodržování etických principů při přípravě vysokoškolských závěrečných prací“.

23.9.2020

Datum převzetí zadání


Podpis studenta(ky)

SPECIFIKACE ZADÁNÍ

Jméno diplomanta: Bc. Liya Gaynutdinova

Název diplomové práce: Micromechanical Parameter Identification using the Bayes Method

Základní část: Teoretický rámec pro řešenou problematiku podíl: 70 %

Formulace úkolů: Seznámení se s problematikou korelace digitálního obrazu

Formulace inverzní úlohy

Řešení inverzní úlohy s využitím Bayesova přístupu

Metodické vedení při psaní diplomové práce a prezentaci výsledků

Podpis vedoucího DP:.....

Datum: 22.9.2020

Případné další části diplomové práce (části a jejich podíl určí vedoucí DP):

2. Část: Výpočetní rámec pro řešenou problematiku podíl: 30 %

Konzultant (jméno, katedra): Ing. Jan Havelka, Ph.D., Experimentální centrum

Formulace úkolů: Diskretizace úlohy pomocí metody konečných prvků

Implementace bayesovského algoritmu v MATLABu, otestování algoritmu

Studium vlivu aproximace okrajových podmínek

Podpis konzultanta:.....

Datum: 22.9.2020

3. Část: _____ podíl: _____ %

Konzultant (jméno, katedra): _____

Formulace úkolů: _____

Podpis konzultanta:.....

Datum:

4. Část: _____ podíl: _____ %

Konzultant (jméno, katedra): _____

Formulace úkolů: _____

Podpis konzultanta:.....

Datum:

Poznámka:

Zadání včetně vyplněných specifikací je nedílnou součástí diplomové práce a musí být přiloženo k odevzdané práci. (Vyplněné specifikace není nutné odevzdat na studijní oddělení spolu s 1. stranou zadání již ve 2. týdnu semestru)

Affidavit

I declare that I have developed the diploma thesis independently and all used sources and literature are recorded in the list of cited literature.

I have no objection to the use of this school work in the sense of §60 of Act No. 121/2000 Coll. on Copyright, on Rights Related to Copyright and on Amendments to Certain Acts (Copyright Act).

Čestné prohlášení

Prohlašuji, že jsem diplomovou práci vypracovala samostatně a všechny použité prameny a literatura jsou uvedeny v seznamu citované literatury.

Nemám námitek proti použití tohoto školního díla ve smyslu §60 Zákona č. 121/2000 Sb. o právu autorském, o právech souvisejících s právem autorským a o změně některých zákonů (autorský zákon).

In Prague/V Praze dne 25. 12. 20

.....
signature/podpis

Acknowledgments

I would like to express my gratitude to this thesis supervisor prof. Ing. Jan Zeman, Ph.D., for giving me the chance to work on this project and bringing together an excellent team of researchers including doc. RNDr. Ivana Pultarová, Ph.D., Ing. Ondřej Rokoš, Ph.D., Ing. Jan Havelka, Ph.D., all of whom brought valuable contributions to this work from start to finish. Special thanks goes to Ondřej Rokoš for our many discussions over MS Teams and e-mail and whose input to this thesis is indispensable.

Anotace

Táto diplomová práca je v formě odborného článku. Uvažuje se problém identifikace mikromechanického parametru pomocí virtuálního testu, kde se jako metoda měření celého pole používá digitální korelace obrazů (DIC). távající deterministický přístup k identifikaci parametrů ve formě integrované digitální korelace obrazu (IDIC) se dříve ukázal jako příliš citlivý na chyby hraničních dat. V této práci je navržen stochastický přístup, který využívá metodu vzorkování Markov Chain Monte Carlo, Metropolisův-Hastingsův algoritmus (MHA). Identifikované parametry spadají do dvou charakteristických skupin: materiálové parametry a parametry okrajových podmínek. Nejprve se uvede MHA, který identifikuje pouze materiálové parametry s fixovanými okrajovými podmínkami, pro náhodné a systematické chyby v okrajových podmínkách je kvantifikována a porovnána s IDIC. Poté, co jsou navrženy dva různé způsoby parametrizace okrajových podmínek pro účely vzorkování, je metoda porovnána s novou metodou integrované digitální korelace obrazů obohacené o hranici (Boundary Enriched Digital Image Correlation). Všechny metody jsou testovány pomocí virtuálního experimentu, který využívá Neo-Hookeův hyperelastický mikromechanický model, diskretizovaný metodou konečných prvků. Je uvažováno o výhodách a úskalích všech studovaných algoritmů.

Klíčová slova

Digitální korelace obrazu, Identifikace parametrů, Virtuální experiment, Mikromechanika, Inverzní metody, Metropolisův-Hastingsův algoritmus

Annotation

This master's thesis is presented in the style of a scientific paper. The problem of micromechanical parameter identification in a heterogeneous material is considered, where Digital Image Correlation (DIC) method is used as a full-field measurement technique. The existing deterministic approach to parameter identification in the form of Integrated DIC (IDIC) was shown to be overly sensitive to boundary data errors. In this work, the stochastic approach is proposed, which employs a Markov Chain Monte Carlo sampling method, i. e. Metropolis-Hastings algorithm (MHA). The identified parameters fall into two distinctive groups: material parameters and boundary conditions parameters. First, the MHA that only identifies the material parameters with fixed boundary conditions is considered, and its sensitivity with respect to random and systematic errors in the boundary conditions is quantified and compared to the IDIC. MHA's parameter field is then expanded with two different ways of approximating the boundary conditions, and the method is compared to the Boundary Enriched IDIC. All methods are tested with a virtual experiment that employs a Neo-Hookean hyperelastic micromechanical model, discretised with the Finite Elements Method. Benefits and pitfalls of all studied algorithms are discussed.

Keywords

Digital Image Correlation, Parameter identification, Virtual experiment, Micromechanics, Inverse methods, Metropolis-Hastings algorithm

Micromechanical Parameter Identification Using Bayes Method

L. Gaynutdinova^{a,*}, O. Rokoš^b, J. Zeman^a, J. Havelka^a, I. Pultarová^a

^a*Czech Technical University in Prague, 166 29 Prague 6, Thákurova 2077/7, Czech Republic*

^b*Eindhoven University of Technology, 5600 MB Eindhoven, P.O. Box 513, The Netherlands*

Abstract

Micromechanical parameters are required for constitutive laws that help to predict complex physical processes in materials, such as strain localisation, plasticity, delamination and cracks. The problem of micromechanical parameter identification in a heterogeneous material is considered, where Digital Image Correlation (DIC) method is used as a full-field measurement technique. The existing deterministic approach to parameter identification in the form of Integrated DIC (IDIC) was shown to be overly sensitive to boundary data errors. In this work, the stochastic approach is proposed, which employs a Markov Chain Monte Carlo sampling method, i.e. the Metropolis–Hastings algorithm (MHA). The identified parameters fall into two distinct groups: material and boundary conditions parameters. First, the MHA that only identifies the material parameters with fixed boundary conditions is considered, and its sensitivity with respect to random and systematic errors in the boundary conditions is quantified and compared to the IDIC. MHA’s parameter field is then expanded with two different ways of approximating the boundary conditions, and the method is compared to the Boundary Enriched IDIC. All methods are tested with a virtual experiment that employs a Neo-Hookean hyperelastic micromechanical model, discretised with the Finite Elements Method. Benefits and pitfalls of all studied algorithms are discussed.

Keywords: Digital Image Correlation, Parameter identification, Virtual experiment, Micromechanics, Inverse methods, Metropolis–Hastings algorithm

*Corresponding author.

Email addresses: liya.gaynutdinova@fsv.cvut.cz (L. Gaynutdinova), o.rokos@tue.nl (O. Rokoš), jan.zeman@cvut.cz (J. Zeman), jan.havelka@fsv.cvut.cz (J. Havelka), ivana.pultarova@cvut.cz (I. Pultarová)

Contents

1	Introduction	16
2	Parameter Identification Using DIC	18
2.1	Global Digital Image Correlation	19
2.2	Integrated Digital Image Correlation	19
2.3	Boundary Enriched IDIC	19
3	Stochastic Approach to Parameter Identification	20
3.1	Parameter Estimation in Bayesian Statistics	21
3.2	Metropolis–Hastings Algorithm	22
4	The Underlying Mechanical Model	23
4.1	Geometry	23
4.2	Constitutive Model	24
4.3	Applied Boundary Conditions	25
4.4	Discretisation and Solution	25
5	Robustness of MHA and IDIC with Respect to Fixed Errors in Applied Boundary Conditions	27
5.1	Sensitivity with Respect to Systematic Errors in Applied Boundary Conditions	27
5.2	Sensitivity with Respect to Random Perturbations in Applied Boundary Conditions	28
6	Parametrisation of Applied Kinematic Boundary Conditions	32
6.1	Finite Element Basis	33
6.2	Comparison of MHA to BE-IDIC	39
6.3	Parametrisation of the Noise Present in Applied Kinematic Boundary Conditions	45
7	Summary and Conclusions	50
8	Appendix	54

1. Introduction

Often the only way we can correctly interpret the behaviour of real materials with heterogeneous structure is by observing them on a microscopic level, so we can account for strain localisation, plasticity, delamination and cracks. Thus the need in non-intrusive, non-contact measurement methods that provide continuous data, as opposed to local measurements, led to full-field measurement techniques becoming a staple in experimental mechanics, even before the contemporary computer technology, e.g. X-ray radiography for strain measurements in the 1960s, False Relief Stereophotogrammetry (FRS) for direct measurement of deformations and Moiré Interferometry for strain analysis throughout 1970s and 1980s (Avril et al., 2008). Nevertheless, digital imaging made possible a highly accurate method such as Digital Image Correlation (DIC), which is essentially a mathematical tool for assessing the spatial transformation between two digital images. In practice, DIC is implemented as a computer program that allows regions of a photographed object to be tracked automatically from one image to the next, from which displacements can be inferred. Affordability and availability of the equipment and computer programs contributed to this method's popularity (Viggiani and Hall, 2008).

DIC technique is typically used as a measuring tool for identifying micromechanical parameters, leading to methods such as the Integrated Digital Image Correlation (IDIC) (Leclerc et al., 2009). The method relies on the minimisation of the difference between two images of a microstructure captured during an experiment i.e. in a reference and a deformed configuration. Although scanning the whole specimen is possible, it is time consuming and computationally expensive. That is why only a subdomain of the specimen is typically considered, referred to as the Microstructural Volume Element (MVE). This approach, however, typically leads to problems with highly heterogeneous boundary conditions.

To capture the displacements associated with the micro-level processes, the size of a digital pixel associated with DIC must often approach the order of nanometers. While modern commercially available optical microscopes are able to provide the needed resolution, the problem lies in the fact that magnification leaves the applied load outside the camera's Field of View (FOV). On the other hand, high accuracy in boundary conditions prescribed to the MVE model is crucial (Rokoš et al., 2018), as even small errors undermine the accuracy of the identified parameters.

The most accurate way to establish MVE boundary conditions, according to Shakoor et al. (2017), is to employ Global DIC (GDIC). The displacements are identified on the whole specimen and are subsequently interpolated as boundary conditions for IDIC. In general (G)DIC introduces: a) kinematic smoothing effect when large elements or globally supported polynomials are used; b) random errors when rela-

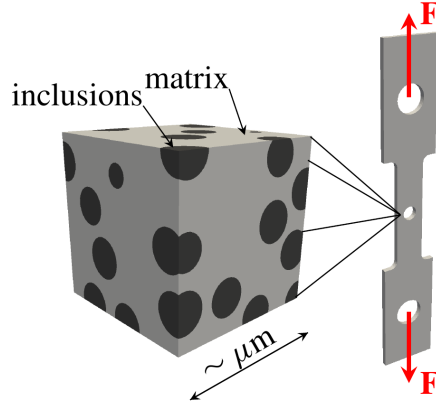


Figure 1: Scheme of the virtual experiment. A microscopic specimen is subjected to tensile or shear load, and the displacements of the heterogeneous structure are observed with optical and scanning electron microscopy.

tively small elements or locally supported interpolation functions are used. Because boundary conditions of the microstructure are kept fixed during the IDIC parameter identification procedure, the microstructure model compensates by adjusting the material parameters, causing inaccurate identification of these parameters (Ruybalid et al., 2017). The approach proposed by Rokoš et al. (2018), referred to as Boundary-Enriched IDIC (BE-IDIC), incorporates all Degrees of Freedom (DOFs) associated with boundary conditions in the IDIC procedure. The method significantly improves the accuracy of the identified parameters while maintaining robustness with respect to image noise. The improved accuracy, however, comes with a price of higher computational and memory requirements.

The aforementioned techniques rely on deterministic optimisation methods, such as the Gauss–Newton algorithm. This article proposes a stochastic method for the parameter identification, namely the Metropolis–Hastings algorithm (MHA), for the minimisation process, while using DIC as the measurement technique. The key difference from the described deterministic methods is that stochastic inversion allows to infer probability distributions of the unknown model parameters instead of single values, treating each iteration as an experimental measurement. Although computationally costly, the dimensionality of the problem does not have a big impact on the calculation time.

In the next section the relevant background on DIC and deterministic methods is given, followed by the description of the stochastic method in Section 3. Section 4 describes the underlying mechanical model and employed virtual experiments. In

Section 5, the method’s sensitivity with respect to random and systematic errors in the boundary conditions are quantified and compared to IDIC. The following section introduces the parametrisation of applied boundary conditions, and the resulting MHA with boundary DOFs is compared to BE-IDIC. In the penultimate section a new way of incorporating boundary DOFs through noise parametrisation is proposed. The takeaways from the numerical experiments are then summarised in the last section with the outlook on further research.

Throughout this article, the weight and style of the font used to render a variable indicates its type: scalar variables are denoted using an italic font, array variables are denoted using a sans serif font, and vectors and tensors are rendered in a boldface font.

2. Parameter Identification Using DIC

A mechanical test is considered, as outlined in Fig. 1. DIC is used to assess spatial transformations before and after loading the specimen. A region of a photographed domain is tracked between the images, which allows us to infer the displacement field (Roux and Hild, 2006). A camera takes snapshots of a Region of Interest (ROI), which lies within the MVE. The camera’s static FOV (Fig. 2) is chosen so that the ROI remains inside it after deformation. The images are stored as integer-valued matrices for both initial and deformed configuration, where each integer is associated with a pixel and denotes its brightness.

The goal is to identify the set of material parameters used in the virtual test. Then the problem is to find a vector $\boldsymbol{\lambda} \in \mathbb{R}^{n_\lambda}$ that minimises the difference between the values in the reference image and in the corresponding material points in the deformed image in the least squares sense based on a displacement field i.e.

$$\boldsymbol{\lambda} \in \underset{\hat{\boldsymbol{\lambda}} \in \mathbb{R}^{n_\lambda}}{\arg \min} \mathcal{R}_{\text{DIC}}(\hat{\boldsymbol{\lambda}}), \quad (1)$$

where \mathcal{R}_{DIC} is a non-convex cost functional

$$\mathcal{R}_{\text{DIC}}(\hat{\boldsymbol{\lambda}}) = \frac{1}{2} \int_{\Omega_{\text{ROI}}} \left[f(\mathbf{X}) - g(\mathbf{X} + \mathbf{u}(\mathbf{X}, \hat{\boldsymbol{\lambda}})) \right]^2 d\mathbf{X} \quad (2)$$

where $\mathbf{u}(\mathbf{X}, \hat{\boldsymbol{\lambda}}) = [u_1(\mathbf{X}, \hat{\boldsymbol{\lambda}}), u_2(\mathbf{X}, \hat{\boldsymbol{\lambda}})]^\top$ is an approximate displacement field, $\mathbf{X} = [X_1, X_2]^\top \in \Omega_{\text{MVE}} \subset \mathbb{R}^2$ stores the material coordinates in the reference configuration, $f(\mathbf{X})$ represents the initial image, $g(\mathbf{X} + \mathbf{u}(\mathbf{X}, \hat{\boldsymbol{\lambda}}))$ is the deformed image mapped onto the initial configuration. The hat ($\hat{\bullet}$) denotes variables with arbitrary admissible values, whereas the absence of hats indicates minimisers. The variable $\hat{\boldsymbol{\lambda}}$ is a column vector that can also store kinematic DOFs as well as material constants.

2.1. Global Digital Image Correlation

GDIC is used to prescribe Dirichlet boundary conditions to a given MVE. The displacement field is obtained through the minimisation of a functional over subspace of functions $\boldsymbol{\psi}(\mathbf{X})$ (Neggers et al., 2014):

$$\mathbf{u}(\mathbf{X}) \approx \mathbf{u}(\mathbf{X}, \hat{\boldsymbol{\lambda}}) = \sum_{i=1}^{n_\lambda} \boldsymbol{\psi}_i(\mathbf{X}) \hat{\lambda}_i \quad (3)$$

where $\boldsymbol{\psi}_i(\mathbf{X})$, $i = 1, \dots, n_\lambda$ are vector-valued interpolation (or basis) functions (and thus also sensitivity fields), usually expressed in terms of globally- or locally-supported polynomials.

2.2. Integrated Digital Image Correlation

Integrated Digital Image Correlation (IDIC) is a method proposed by Roux and Hild (2006) to solve Eq. (1), where a standard Gauss–Newton algorithm can be used to minimise Eq. (2) and is described in detail in Rokoš et al. (2018).

The displacement field $\mathbf{u}(\mathbf{X}, \hat{\boldsymbol{\lambda}})$ is then obtained by minimising the squared residual (cost functional) with respect to $\boldsymbol{\lambda}$:

$$\hat{\boldsymbol{\lambda}} = \arg \min_{\hat{\boldsymbol{\lambda}}} \mathcal{R}_{\text{DIC}}(\hat{\boldsymbol{\lambda}}), \quad (4)$$

resulting in mechanical system for IDIC with a solution:

$$\mathbf{u}(\mathbf{X}, \hat{\boldsymbol{\lambda}}) \in \arg \min_{\hat{\mathbf{u}}(\mathbf{X}, \boldsymbol{\lambda}) \in \mathcal{U}(\hat{\boldsymbol{\lambda}})} \mathcal{E}(\hat{\mathbf{u}}(\mathbf{X}, \boldsymbol{\lambda}), \hat{\boldsymbol{\lambda}}), \quad (5)$$

that is specified by its stored energy \mathcal{E} and a proper function space \mathcal{U} (Evans, 2010), $\hat{\mathbf{u}}(\mathbf{X}, \hat{\boldsymbol{\lambda}})$ is usually a solution discretised with the Finite Elements Method (FEM). \mathcal{U} and \mathcal{E} depend on $\hat{\boldsymbol{\lambda}}$, because $\boldsymbol{\lambda}$ stores not only material constants, but also kinematic variables such as prescribed boundary conditions.

2.3. Boundary Enriched IDIC

BE-IDIC (Rokoš et al., 2018) is an IDIC methodology that considers material parameters $\hat{\boldsymbol{\lambda}}_{\text{mat}}$ as well as the vector of displacements associated with all the boundary displacements $\hat{\boldsymbol{\lambda}}_{\text{kin}}$ as unknowns, i.e.

$$\hat{\boldsymbol{\lambda}} = [\hat{\boldsymbol{\lambda}}_{\text{mat}}^T, \hat{\boldsymbol{\lambda}}_{\text{kin}}^T]^T, \quad (6)$$

where

$$\widehat{\boldsymbol{\lambda}}_{\text{mat}} = [G_1, K_1, \dots]^T, \quad (7)$$

$$\widehat{\boldsymbol{\lambda}}_{\text{kin}} = \widehat{\mathbf{u}}(\mathbf{X}), \quad \mathbf{X} \in \partial\Omega_{\text{MVE}}, \quad (8)$$

and G_i, K_i are the constitutive equation parameters. The cost functional $\mathcal{R}(\widehat{\boldsymbol{\lambda}})$, defined in Eq. (2), is then minimised following the standard IDIC procedure. The assets and disadvantages of the BE-IDIC method are described in [Rokoš et al. \(2018\)](#).

3. Stochastic Approach to Parameter Identification

As was described above in Section 2.2, the deterministic approach in the form of IDIC is a relatively computationally inexpensive method that provides a single value for identified parameters. On the other hand, obtaining precise enough MVE boundary conditions is a challenge on its own, and the GDIC-IDIC method is overly sensitive to the accuracy of the boundary conditions, because the errors that occurred during GDIC phase become fixed.

For successful identification process, one has to separate occurring uncertainties into two basic groups ([Oberkampf et al., 2002](#)). First group, called epistemic uncertainty, derives from lack of knowledge of the system or the environment. Material parameters and boundary conditions fall into this category in our case. This type of uncertainty is reducible by adding new information, i.e. by performing more tests with parameters $\widehat{\boldsymbol{\lambda}}$, one can obtain better estimates. The second group is called aleatory uncertainty, or simply variability, and is irreducible. It represents an inherent variation associated with the physical system or the environment under consideration. It is important to distinguish both classes of uncertainties from errors — modelling inaccuracies, identifiable or knowable a priori, stemming e.g. from FEM discretisation, solution approximation or GDIC interpolation.

Bayesian probability has been used for epistemic uncertainty, and it takes a subjective view of probability as a measure of degree of belief in a hypothesis. Bayesian methods allow us to update the probabilities as we gather more data (Bayesian inference). The final answer to the parameter identification problem is then a posterior distribution, as opposed to a single value obtained from the deterministic methods. Additionally, working with prior parameter distribution could regularise the problem and negate the sensitivity for errors. That is why employing a stochastic method to this problem of parameter identification is potentially beneficial and has been already used, in fact, for inverse problems in PDEs with heterogeneous materials ([Blaheta et al., 2018](#); [Janouchová and Kučerová, 2018](#)).

3.1. Parameter Estimation in Bayesian Statistics

In the Bayesian statistics, parameter estimation is done by testing numerous hypotheses. To find the posterior probability density for a continuous set of possibilities $\boldsymbol{\theta}$, we use this form of Bayes' rule, see [Stuart and Ord \(1994\)](#):

$$p(\boldsymbol{\theta}|\mathbf{x}) \propto p(\boldsymbol{\theta})p(\mathbf{x}|\boldsymbol{\theta}), \quad (9)$$

where $p(\boldsymbol{\theta}|\mathbf{x})$ is the posterior probability, $p(\boldsymbol{\theta})$ is the prior probability, which describes the distribution of $\boldsymbol{\theta}$ before \mathbf{x} is observed, and $p(\mathbf{x}|\boldsymbol{\theta})$ is the likelihood function, which is the probability of observing \mathbf{x} , given $\boldsymbol{\theta}$. The data set \mathbf{x} will then consist of individual tests that result in observed images $f(\mathbf{X})$ and $g(\mathbf{X})$ provided by DIC. Supposing that the brightness is conserved between two images and omitting the interpolation error, we assume that

$$f(\mathbf{X}) \cong g(\mathbf{X} + \mathbf{u}(\mathbf{X}, \hat{\boldsymbol{\lambda}})).$$

In practice, we work with the discretised version of f and g , which we denote respectively as vectors \mathbf{f} and \mathbf{g} of N_b elements, representing individual pixels. Accounting for the measurement error (i.e. image noise) we write:

$$\mathbf{f}(\mathbf{X}) + \boldsymbol{\eta}(\mathbf{X}) = \mathbf{g}(\mathbf{X} + \mathbf{u}(\mathbf{X}, \hat{\boldsymbol{\lambda}})) + \boldsymbol{\zeta}(\mathbf{X} + \mathbf{u}(\mathbf{X}, \hat{\boldsymbol{\lambda}})), \quad (10)$$

where $\boldsymbol{\eta}$ and $\boldsymbol{\zeta}$ are the random field representing measurement errors, normally distributed with zero mean and variance σ_η^2 , i.e. $\boldsymbol{\eta}, \boldsymbol{\zeta} \in \mathcal{N}(0, \sigma_\eta^2)$. Conversely, Eq. (10) can be written as

$$\mathbf{f}(\mathbf{X}) \cong \mathbf{g}(\mathbf{X} + \mathbf{u}(\mathbf{X}, \hat{\boldsymbol{\lambda}})) + \boldsymbol{\xi}(\mathbf{X} + \mathbf{u}(\mathbf{X}, \hat{\boldsymbol{\lambda}})), \quad \boldsymbol{\xi} \in \mathcal{N}(0, 2\sigma_\eta^2) \quad (11)$$

Let us denote the prior distribution of the parameters $\hat{\boldsymbol{\lambda}} = [\lambda_{\text{mat},1}, \dots, \lambda_{\text{mat},n_{\text{mat}}}, \lambda_{\text{kin},1}, \dots, \lambda_{\text{kin},n_{\text{kin}}}]^\top$ as π_m , $m = 1, \dots, n_\lambda = n_{\text{mat}} + n_{\text{kin}}$, recall Eq. (6). Then, according to Bayes' theorem in Eq. (9), posterior distribution $\pi(\hat{\boldsymbol{\lambda}})$ can be obtained as:

$$\pi(\hat{\boldsymbol{\lambda}}|\mathbf{f}, \mathbf{g}) \propto \pi_m(\hat{\boldsymbol{\lambda}})\pi(\mathbf{f}, \mathbf{g}|\hat{\boldsymbol{\lambda}}) \quad (12)$$

The likelihood $\pi(\mathbf{f}, \mathbf{g}|\hat{\boldsymbol{\lambda}})$ is then computed using the probability density function φ of $\boldsymbol{\xi}$ as:

$$\pi(\mathbf{f}, \mathbf{g}|\hat{\boldsymbol{\lambda}}) \propto \varphi(\mathbf{f}(\mathbf{X}) - \mathbf{g}(\mathbf{X} + \mathbf{u}(\mathbf{X}, \hat{\boldsymbol{\lambda}}))) \quad (13)$$

$$= \frac{1}{\sqrt{2\pi\sigma_\eta^{2N_b}}} \exp\left(\frac{-\|\mathbf{f}(\mathbf{X}) - \mathbf{g}(\mathbf{X} + \mathbf{u}(\mathbf{X}, \hat{\boldsymbol{\lambda}}))\|_2^2}{2\sigma_\eta^2}\right). \quad (14)$$

Considering that the measurement errors mostly stem from the image noise, we set σ_η as 1% of the mean value of f . Now we can compute the approximate probability

$$\pi(\widehat{\boldsymbol{\lambda}}|\mathbf{f}, \mathbf{g}) = C \pi_1(\widehat{\lambda}_1) \cdots \pi_{n_\lambda}(\widehat{\lambda}_{n_\lambda}) \pi(\mathbf{f}, \mathbf{g}|\widehat{\boldsymbol{\lambda}}), \quad (15)$$

where C represents a normalisation constant.

3.2. Metropolis–Hastings Algorithm

Let us look at our problem in Eq. (1) as now having two distinctive sets of parameters: the material parameters $\boldsymbol{\lambda}_{\text{mat}}$ and boundary conditions $\boldsymbol{\lambda}_{\text{kin}}$, recall Eq. (6) and related discussion.

We are, of course, mainly interested in the estimation of the set $\boldsymbol{\lambda}_{\text{mat}}$. While the set $\boldsymbol{\lambda}_{\text{kin}}$ is important to determine the boundary conditions, we are not that interested in its values, so we are going to treat it as a nuisance parameter. To get the marginal posterior distribution $\pi(\boldsymbol{\lambda}_{\text{mat}}|\mathbf{f}, \mathbf{g})$ and not the joint distribution $\pi(\boldsymbol{\lambda}_{\text{mat}}, \boldsymbol{\lambda}_{\text{kin}}|\mathbf{f}, \mathbf{g})$ we are going to use the Markov Chain Monte Carlo (MCMC) sampling. The marginalisation can be done using the sum rule:

$$\pi(\boldsymbol{\lambda}_{\text{mat}}|\mathbf{f}, \mathbf{g}) = \int_{\boldsymbol{\lambda}_{\text{kin}}} \pi(\boldsymbol{\lambda}_{\text{mat}}, \boldsymbol{\lambda}_{\text{kin}}|\mathbf{f}, \mathbf{g}) d\boldsymbol{\lambda}_{\text{kin}}. \quad (16)$$

To evaluate this integral, the Metropolis–Hastings algorithm (MHA) will be used.

In MHA (Lee, 2012), we start with an initial sample $\tilde{\boldsymbol{\lambda}}^i$ and set it as the current state $\widehat{\boldsymbol{\lambda}}^i = \tilde{\boldsymbol{\lambda}}^i$. Then each new proposal $\tilde{\boldsymbol{\lambda}}^{i+1}$ is generated based on the proposal distribution q which is symmetric in the sense that $q(\tilde{\boldsymbol{\lambda}}^i|\tilde{\boldsymbol{\lambda}}^{i+1}) = q(\tilde{\boldsymbol{\lambda}}^{i+1}|\tilde{\boldsymbol{\lambda}}^i)$ for all $\tilde{\boldsymbol{\lambda}}^i, \tilde{\boldsymbol{\lambda}}^{i+1} \in \mathbb{R}^{M=n_{\text{mat}}+n_{\text{kin}}}$. Usually q is Gaussian. In the numerical experiments, we will assume that its mean is zero and its variance is chosen arbitrarily as σ_q^2 . The newly proposed state $\tilde{\boldsymbol{\lambda}}^{i+1}$ is then accepted with the probability of $\min(1, p)$, where

$$p = \frac{\pi(\tilde{\boldsymbol{\lambda}}^{i+1}|\mathbf{f}, \mathbf{g})}{\pi(\widehat{\boldsymbol{\lambda}}^i|\mathbf{f}, \mathbf{g})}. \quad (17)$$

This is usually implemented by generating a uniformly randomly distributed variable $\kappa \in \mathcal{U}(0, 1)$. If $\kappa < p$, then $\tilde{\boldsymbol{\lambda}}^{i+1}$ is accepted i.e. $\widehat{\boldsymbol{\lambda}}^{i+1} = \tilde{\boldsymbol{\lambda}}^{i+1}$, otherwise $\tilde{\boldsymbol{\lambda}}^{i+1}$ is rejected, i.e. $\widehat{\boldsymbol{\lambda}}^{i+1} = \widehat{\boldsymbol{\lambda}}^i$. Continuing this way, one obtains a sequence $\widehat{\boldsymbol{\lambda}}^j$, $j = 1, 2, \dots, N$. After discarding the first N_0 elements (the so called burn-in), one can finally obtain approximation of marginal or joint posterior distributions of identified parameters $\boldsymbol{\lambda}$ as distributions of $\widehat{\lambda}_m^j$, $j = N_0 + 1, \dots, N$, for $m = 1, \dots, n_\lambda$.

Algorithm 1: Metropolis–Hastings algorithm to sample posterior distributions in Eq. (16)

1. Draw initial state $\tilde{\boldsymbol{\lambda}}^1 \in \mathbb{R}^M$.
Set $\widehat{\boldsymbol{\lambda}}^1 = \tilde{\boldsymbol{\lambda}}^1$.
2. For $i = 2, 3, \dots, N$ do:
 - (a) draw proposal $\tilde{\boldsymbol{\lambda}}^{i+1} \sim \mathcal{N}(\widehat{\boldsymbol{\lambda}}^i, \sigma_q^2)$
 - (b) set $p = \pi(\tilde{\boldsymbol{\lambda}}^{i+1} | \mathbf{f}, \mathbf{g}) / \pi(\widehat{\boldsymbol{\lambda}}^i | \mathbf{f}, \mathbf{g})$
 - (c) draw $\kappa \sim \mathcal{U}(0, 1)$
 - (d) if $\kappa < p$ set $\tilde{\boldsymbol{\lambda}}^{i+1} = \tilde{\boldsymbol{\lambda}}^{i+1}$ (i.e. accept $\tilde{\boldsymbol{\lambda}}^{i+1}$), else set $\widehat{\boldsymbol{\lambda}}^{i+1} = \widehat{\boldsymbol{\lambda}}^i$ (i.e. reject $\tilde{\boldsymbol{\lambda}}^{i+1}$)
3. Discard $\widehat{\boldsymbol{\lambda}}^1, \widehat{\boldsymbol{\lambda}}^2, \dots, \widehat{\boldsymbol{\lambda}}^{N_0}$ (burn in).
4. Compute estimates of parameter characteristics from $\widehat{\boldsymbol{\lambda}}^{N_0+1}, \dots, \widehat{\boldsymbol{\lambda}}^N$.

4. The Underlying Mechanical Model

4.1. Geometry

The adopted virtual experiment is performed on a specimen with prescribed material parameters $\boldsymbol{\lambda}_{\text{mat,ref}}$. The specimen in question is assumed on a domain Ω_{DNS} , having the size of a 20×20 square, with a heterogeneous structure shown in Fig. 2. The microstructure consists of spatially randomised non-intersecting stiff circular inclusions with a diameter $d = 1$, and a surrounding compliant matrix. Although all geometric properties are dimensionless, they can be scaled to μm .

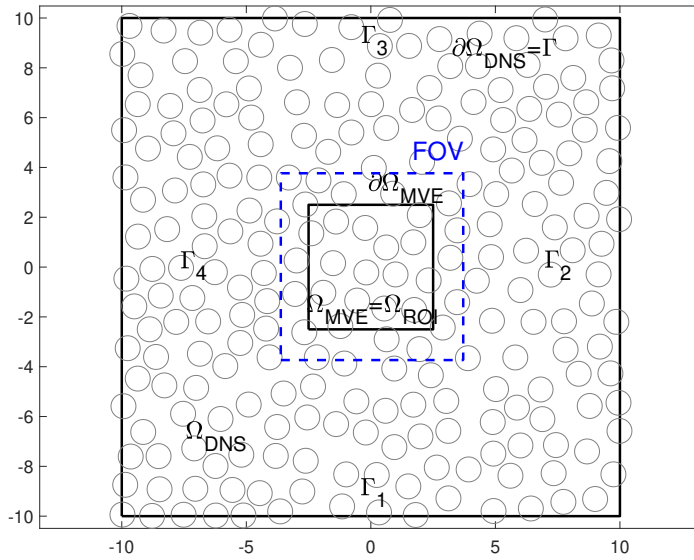


Figure 2: Sketch of the specimen's square domain Ω_{DNS} , microstructural volume element Ω_{MVE} and the FOV. The domain consists of stiff circular fibres of diameter $d = 1$, embedded in a compliant matrix.

4.2. Constitutive Model

The material of the specimen is assumed to be nonlinearly elastic. In particular, a compressible Neo–Hookean hyperelastic material is adopted, specified by the following elastic energy density

$$W_\alpha(\mathbf{F}) = \frac{1}{2}G_\alpha(\bar{I}_1(\mathbf{F}) - 3) + \frac{1}{2}K_\alpha(\ln J(\mathbf{F}))^2, \quad (18)$$

where $\mathbf{u}(\mathbf{X})$ is a displacement field, \mathbf{F} is the deformation gradient tensor, $J(\mathbf{F}) = \det \mathbf{F}$, $\bar{I}_1(\mathbf{F}) = J^{-\frac{2}{3}} \text{tr}(\mathbf{C})$ is the first modified invariant of the right Cauchy–Green deformation tensor $\mathbf{C} = \mathbf{F}^\top \mathbf{F}$. Individual materials are distinguished by the subscript α , $\alpha = 1$ corresponds to the matrix and $\alpha = 2$ to the inclusions. The reference value of the material parameter is presented in Tab. 1, expressed as a function of the material contrast ratio $\varrho > 1$. Throughout all experiments in this work, the contrast ratio is set for $\varrho = 4$. Because Dirichlet boundary conditions are applied on the entire boundary of the MVE, $\partial\Omega_{\text{MVE}}$, only material parameter ratios can be obtained with the IDIC procedure. That is why one needs to fix one of the parameters to an arbitrary value (exact in our case of virtual experiments) for normalisation purpose, and identify the remaining parameters relative to that reference value. The fixed material parameter can be estimated by other means, i.e. a force-based mechanical test or from reliable experimental sources.

Physical parameters	Matrix ($\alpha = 1$)	Inclusions ($\alpha = 2$)
Shear modulus, G_α	1	ϱ
Bulk modulus, K_α	3	3ϱ
Poisson's ratio, $\nu_\alpha = \frac{3K_\alpha - 2G_\alpha}{2(3K_\alpha + G_\alpha)}$	0.35	0.35

Table 1: Material parameters λ_{ref} .

The total elastic stored energy of the entire system reads:

$$\mathcal{E} = \int_{\Omega} (1 - \chi(\mathbf{X}))W_1[\mathbf{I} + \nabla\mathbf{u}(\mathbf{X})] + \chi(\mathbf{X})W_2[\mathbf{I} + \nabla\mathbf{u}(\mathbf{X})]d\mathbf{X} \quad (19)$$

where $\chi(\mathbf{X})$ is an indicator function for the inclusions respectively, i.e. $\chi = 1$ inside all inclusions and $\chi = 0$ inside the matrix.

4.3. Applied Boundary Conditions

Let us denote each side of the boundary of Ω_{DNS} , $\partial\Omega_{DNS} = \Gamma$, as Γ_i , $i = 1, \dots, 4$, see Fig. 2. Two virtual mechanical tests are considered, one to introduce tension and another to introduce shear. Both are referred to as Direct Numerical Simulations (DNS), and are used to provide the reference for the mechanical behaviour of the system. The displacements prescribed at the specimen's boundary are

$$\mathbf{u}(\mathbf{X}) = (\overline{\mathbf{F}} - \mathbf{I})\mathbf{X}, \quad \mathbf{X} \in \Gamma_2 \cup \Gamma_4, \quad (20)$$

$$\overline{\mathbf{F}} = \mathbf{I} + 0.1\mathbf{e}_1 \otimes \mathbf{e}_1, \quad \text{for tension}, \quad (21)$$

$$\overline{\mathbf{F}} = \mathbf{I} + 0.1\mathbf{e}_2 \otimes \mathbf{e}_1, \quad \text{for shear}, \quad (22)$$

where $\mathbf{e}_1 = (1, 0)^\top$ and $\mathbf{e}_2 = (0, 1)^\top$, while Γ_1 , Γ_3 are left as free edges.

4.4. Discretisation and Solution

The solution of the mechanical problem in Eq. (5) is computed using the Total Lagrangian formulation (Tadmor et al., 2012), and the weak form of equilibrium equations in the underformed configuration \mathbf{X} . The evolution of the system is solved incrementally, using the standard Newton–Raphson algorithm. The displacement field $\mathbf{u}(\mathbf{X}, \hat{\boldsymbol{\lambda}})$ is discretised with the Finite Element method (FEM), i.e.

$$\hat{\mathbf{u}}(\mathbf{X}, \hat{\boldsymbol{\lambda}}) = \sum_{i=1}^{n_u/2} N_i(\mathbf{X})\hat{\mathbf{u}}_i(\hat{\boldsymbol{\lambda}}), \quad (23)$$

where $\hat{\mathbf{u}} = [\hat{\mathbf{u}}_1^\top, \dots, \hat{\mathbf{u}}_{n_u/2}^\top]^\top \in \mathbb{R}^{n_u}$, $\hat{\mathbf{u}}_i = [\mathbf{u}_1^i, \mathbf{u}_2^i]^\top \in \mathbb{R}^2$, stores horizontal and vertical displacements of the i -th node associated with a FE mesh, whereas $N_i(\mathbf{X})$ are standard FE shape functions.

For the FE solution, both Ω_{DNS} and Ω_{MVE} domains are discretised with the Gmsh mesh generator (Geuzaine and Remacle, 2009), using quadratic iso-parametric triangular elements and the three-point Gaussian quadrature rule to approximate the integrals appearing in the weak form. All calculations were programmed and performed in MATLAB (MathWorks Inc., 2018), using an in-house FEM library for hyperelastic materials, with computationally heavy parts implemented in external C/C++ mex files for efficiency reasons. For the DNS, the fine mesh shown in Fig. 3a is used, and a coarser MVE triangulation can be found in Fig. 3c. Because the reference Poisson's ratios for both materials are significantly smaller than 0.5, and because deformations in the simulations are moderate, incompressibility issues do not occur.

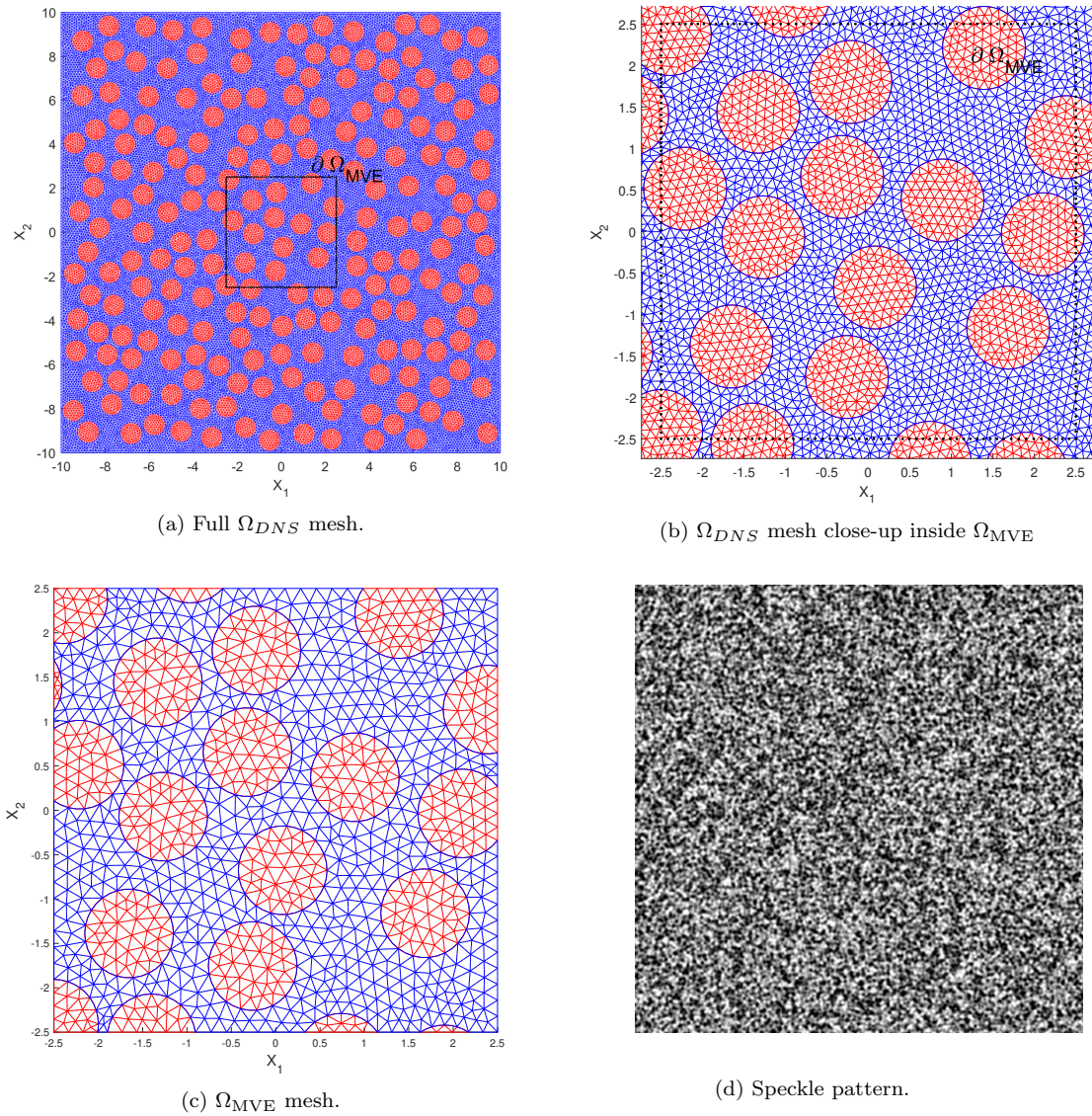


Figure 3: (a) FEM meshes corresponding to the finely discretised full DNS system; (b) close-up on the MVE domain; (c) coarse discretisation of the MVE model, (d) applied speckle pattern.

To track the deformation in a real life experiment, a speckle pattern is applied on the specimen (Jones and Iadicola, 2018). The reference image f , representing the applied speckle pattern, has been adopted from (Bornert et al., 2009) ("medium pattern size"), shown in Fig. 3d. Its resolution is 512×512 pixels inside FOV, which corresponds approximately to 340×340 pixels inside ROI, when ROI is set equal to

MVE. The DNS displacements obtained from all mechanical tests are interpolated from the FE mesh to the regular image mesh, and the resulting displacement fields are used to map the deformed image g into the initial image f . The deformed image is then interpolated at the pixel positions using the bi-cubic polynomial interpolation.

5. Robustness of MHA and IDIC with Respect to Fixed Errors in Applied Boundary Conditions

This section presents several experiments to quantify robustness and accuracy of MHA in comparison with GDIC-IDIC method. The error in boundary conditions is fixed to measure its effect on the material parameter identification. To this end, the effect of systematic errors, like the smoothing of kinematic fields by GDIC, is studied first, followed by the effect of uncorrelated random noise, typically observed in local DIC, or global DIC with a very fine discretisation.

5.1. Sensitivity with Respect to Systematic Errors in Applied Boundary Conditions

The exact DNS displacement field is smoothed as:

$$\tilde{\mathbf{u}}_{\text{DNS}}(\mathbf{X}) = \int_{\Omega} \mathbf{u}_{\text{DNS}}(\mathbf{Y}) h_{\varepsilon}(\mathbf{Y} - \mathbf{X}) d\mathbf{Y}, \quad (24)$$

where h_{ε} is a pillbox-shaped kernel with a dimension-less diameter $\varepsilon \geq 0$ (normalised by the inclusion's diameter $d = 1$). The smoothing effect for the extreme kernel ε can be observed in Fig. 5a. The smoothed data are then prescribed as nodal displacements to the FEM model of MVE:

$$\mathbf{u}_{\text{MVE}}(\mathbf{X}) = \tilde{\mathbf{u}}_{\text{DNS}}(\mathbf{X}), \quad \mathbf{X} \in \partial\Omega_{\text{MVE}}. \quad (25)$$

In Eq. (25), $\tilde{\mathbf{u}}_{\text{DNS}}(\mathbf{X})$, $\mathbf{X} \in \partial\Omega_{\text{MVE}}$, is a column of displacements of $\tilde{\mathbf{u}}_{\text{DNS}}$ evaluated at the MVE boundary nodes. For easier implementation, the integral in Eq. (24) is calculated at discrete pixel positions numerically, while the corresponding displacements are interpolated using a linear interpolation scheme. The relative boundary error due to the smoothing is shown in Fig. 6a. Fig. 4 shows obtained results for both tension and shear, and compares them to the IDIC method.

The MHA with fixed boundary conditions performs almost identically to the IDIC, and eliminating boundary fluctuations by smoothing has a considerable negative impact on the identification accuracy. Non-monotonicity of the identified parameters can be explained by the particular morphology of the microstructure.

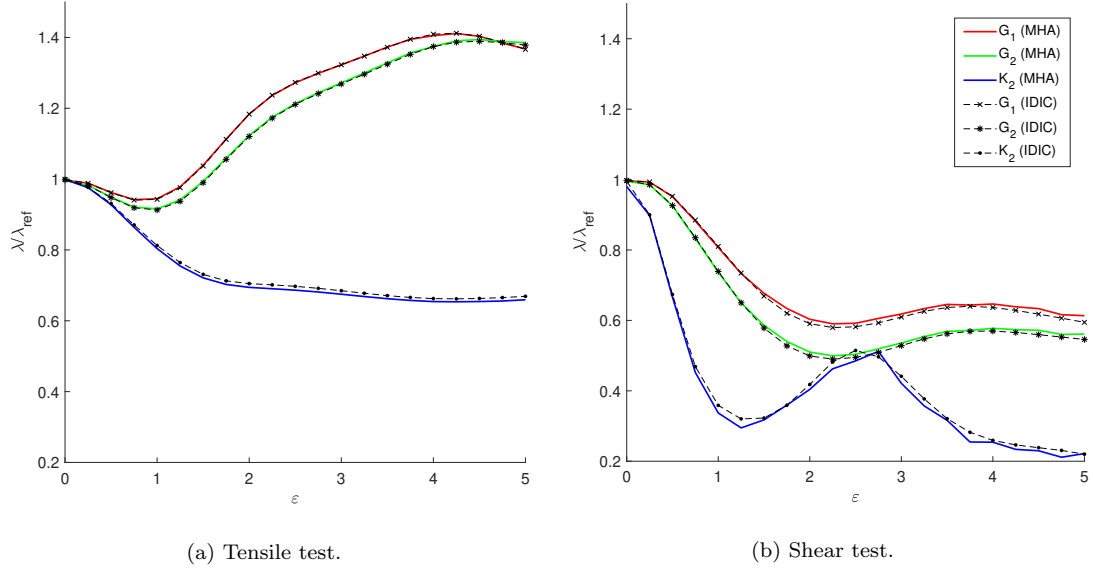


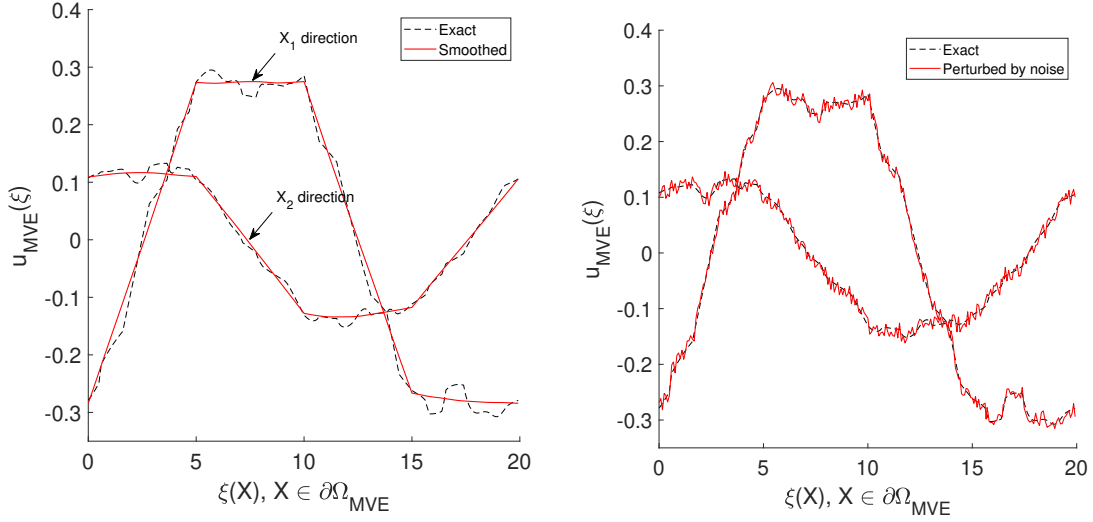
Figure 4: Identified results for MHA compared against the IDIC method, mean values of the posterior distributions. Boundary displacements are smoothed using the pillbox-shaped kernel with the parameter ε and fixed according to Eq. (24), for (a) tensile and (b) shear tests. Parameters identified by MHA correspond to $N = 4\,000$ steps, burn in $N_0 = 2\,000$ steps.

5.2. Sensitivity with Respect to Random Perturbations in Applied Boundary Conditions

To quantify the effect of random noise in boundary conditions on the material parameter identification, the following test is performed. The Dirichlet boundary conditions are obtained by interpolating the DNS displacements at the nodal positions of the MVE boundary $\partial\Omega_{\text{MVE}}$. Then uncorrelated random noise is superimposed on the boundary displacement, i.e.

$$\mathbf{u}_{\text{MVE}}(\mathbf{X}) = \mathbf{u}_{\text{DNS}}(\mathbf{X}) + \sigma \max_{\mathbf{Y} \in \Omega_{\text{MVE}}} (\|\mathbf{u}_{\text{DNS}}(\mathbf{Y})\|_2) \mathfrak{U}, \quad \mathbf{X} \in \partial\Omega_{\text{MVE}}, \quad (26)$$

where $\mathbf{u}_{\text{MVE}}(\mathbf{X})$ is a column matrix storing nodal displacements of the nodes located at the MVE boundary, $\mathbf{u}_{\text{DNS}}(\mathbf{Y})$ denotes their DNS counterparts, $\mathbf{u}_{\text{DNS}}(\mathbf{X})$, $\mathbf{X} \in \partial\Omega_{\text{MVE}}$, is a DNS displacement field considered everywhere inside Ω_{MVE} , \mathfrak{U} is the corresponding column of Independent and Identically Distributed (iid) random variables with uniform distribution over $[-0.5, 0.5]$, and σ is the standard deviation of the random noise in the prescribed boundary conditions.



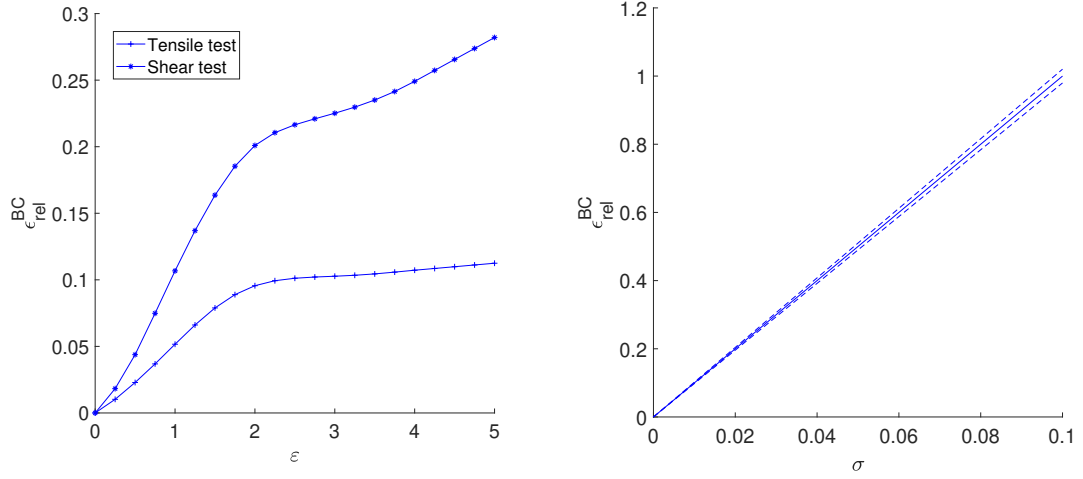
(a) Exact boundary conditions obtained by DNS with smoothed using the pillbox-shaped kernel $\varepsilon = 5$, Section 5.1. (b) Exact boundary conditions obtained by DNS with superimposed noise for $\sigma = 0.1$, Section 5.2.

Figure 5: Examples of substitutions for boundary conditions in different experiments: (a) smoothed boundary conditions, (b) boundary conditions with superimposed noise.

The material parameters are identified for the tensile and shear tests with zero image noise, $\sigma \in [0, 0.1]$, and for 55 Monte Carlo (MC) realisations for each value of σ with noise. An example of boundary data is shown in Fig. 5b. The number of steps for the MHA was set to 4000, prior parameter distributions reflect the assumption that the initial guess is not too far from the actual value, and are set to normal distributions with the mean values equal to $0.9\lambda_{\text{ref},i}$, $i = 1, \dots, 4$. The boundary conditions are fixed, so the dimension of the MHA sampling is reduced only to the material parameter λ_{mat} , thus the sampling is performed in a three-dimensional space. The typical relative error in the prescribed boundary conditions, defined as

$$\epsilon_{\text{rel}}^{\text{BC}} = \frac{\|u_{\text{MVE}}(\mathbf{X}) - u_{\text{DNS}}(\mathbf{X})\|_2}{\|u_{\text{DNS}}(\mathbf{X})\|_2}, \quad \mathbf{X} \in \partial\Omega_{\text{MVE}}, \quad (27)$$

is shown in Fig. 6b.



(a) Relative displacement error $\epsilon_{\text{rel}}^{\text{BC}}$ at $\partial\Omega_{\text{MVE}}$ expressed as a function of the pillbox-shaped kernel size ϵ . (b) Relative displacement error $\epsilon_{\text{rel}}^{\text{BC}}$ of Eq. (27) at $\partial\Omega_{\text{MVE}}$, expressed as a function of noise level σ , mean (solid) \pm standard deviation (dashed).

Figure 6: Relative displacement errors in the boundary conditions for the sensitivity tests, (a) systematic error, (b) mean \pm standard deviation of the random error.

In Fig. 7, the mean values (thick lines) of all parameters with \pm corresponding standard deviations (dashed lines) computed over all MC realisations are shown. This graphical representation is used throughout this work, unless explicitly stated otherwise.

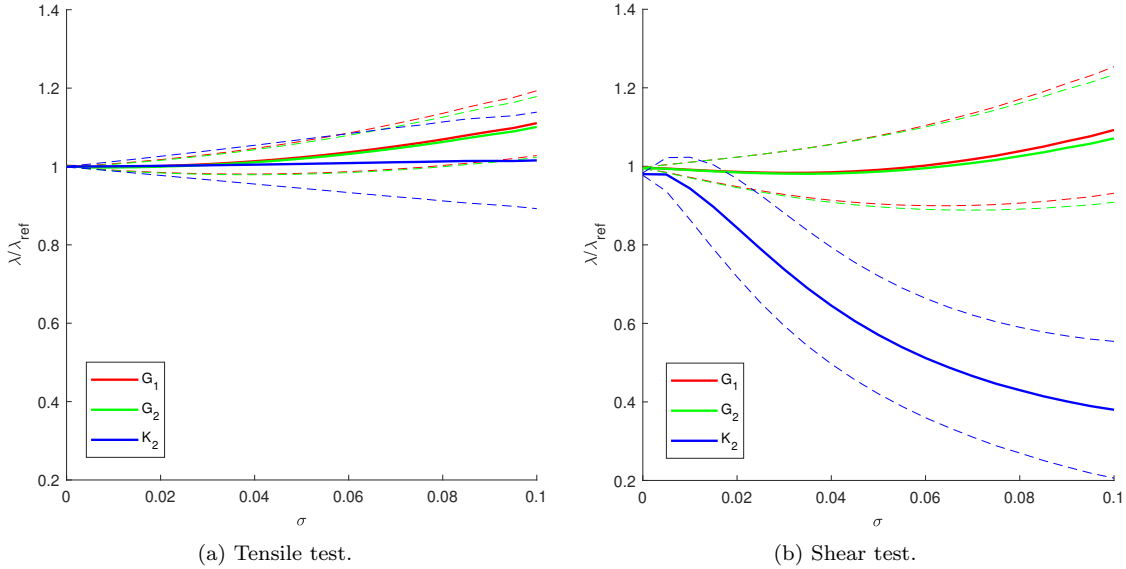


Figure 7: Identified results in the case of random noise in boundary conditions according to Eq. (26), mean (solid) \pm standard deviation (dashed), for increasing $\sigma \in [0, 0.1]$, $N = 4\,000$ steps of MHA, fixed boundary conditions, tensile (a) and shear (b) tests.

As shown in Figs. 8 and 9, MHA (colour lines) again delivers almost identical results to those of IDIC (black lines). The slight deviation for the values of $\sigma > 0.8$ can be explained by the insufficient convergence of the MHA for the higher noise. MHA with fixed boundary error generally has the same robustness as IDIC, meaning that the error in boundary conditions has a significant effect on the identified material parameters' value, especially in the shear test. It should be noted that MHA converges on a very narrow high-probability region with the acceptance rate steadily dropping close to 0% after reaching the point of convergence. Therefore the results are very similar to those of IDIC, even though for the deterministic method the mean and standard deviation are calculated over single values obtained by MC iterations, while MHA provides a dataset of 2 000 values after burn-in for each MC iteration. MHA is also considerably more computationally expensive compared to IDIC, as the solution of the mechanical system must be calculated for each new sample.

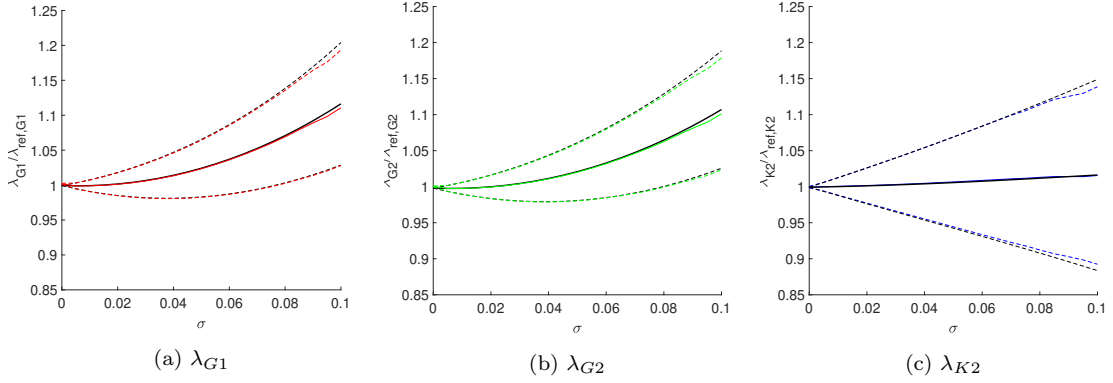


Figure 8: Comparison of the identified (a) matrix shear modulus G_1 , (b) fibre shear modulus G_2 , and (c) fibre bulk modulus K_2 obtained from the tensile test under fixed boundary conditions with IDIC (black) and MHA (color) methods. The means are plotted with solid lines and are complemented with \pm standard deviations (dashed lines). $N = 4\,000$ steps of MHA, increasing $\sigma \in [0, 0.1]$.

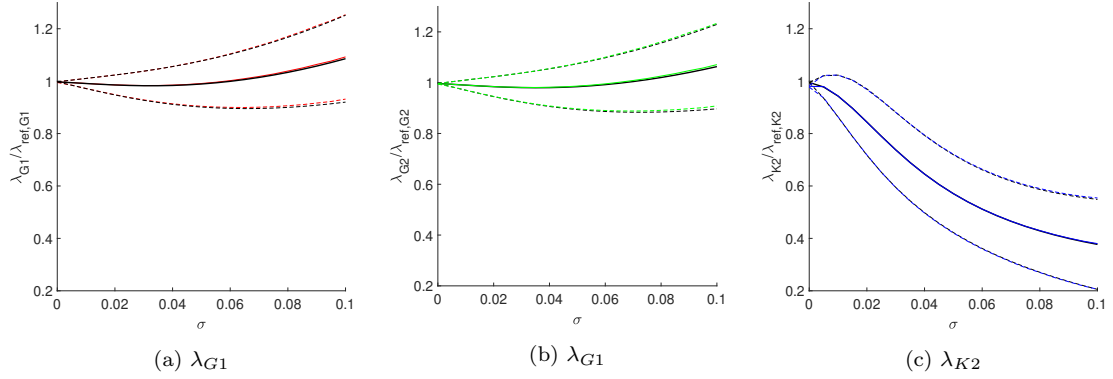


Figure 9: Comparison of the identified (a) matrix shear modulus G_1 , (b) fibre shear modulus G_2 , and (c) fibre bulk modulus K_2 obtained from the shear test under fixed boundary conditions with IDIC (black) and MHA (color) methods. The means are plotted with solid lines and are complemented with \pm standard deviations (dashed lines). $N = 4\,000$ steps of MHA, increasing $\sigma \in [0, 0.1]$.

6. Parametrisation of Applied Kinematic Boundary Conditions

One of the benefits to the Bayesian method is that the number of sampled parameters can be increased to include boundary conditions with no additional computational effort. Probably the most straightforward way to implement this would

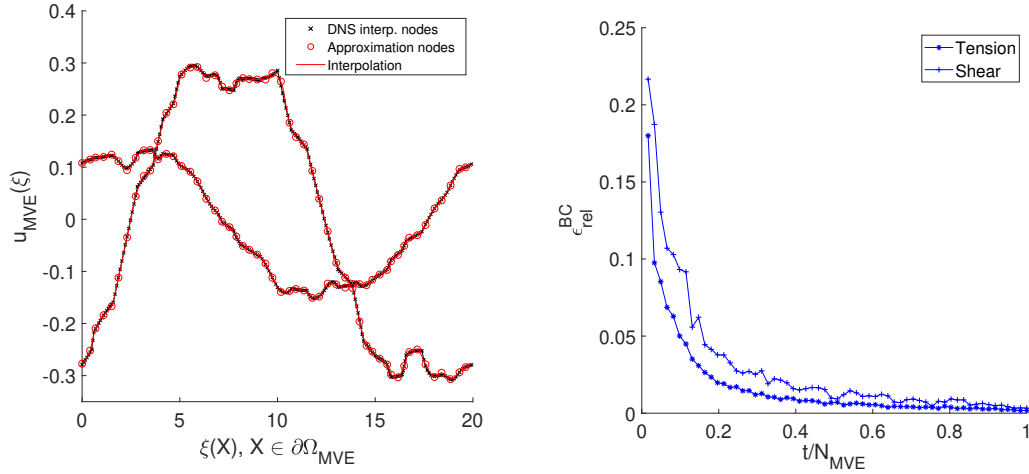
be setting the boundary conditions parameter λ_{kin} as displacements in the FE nodes along $\partial\Omega_{\text{MVE}}$. For the configuration described in Section 4, this would mean adding extra 2×244 parameters, considering that each node stores displacements along $\mathbf{X} = [X_1, X_2]$. While possible, this approach is generally expected to introduce the so-called “curse of dimensionality” (Au and Beck, 2001; Katafygiotis and Zuev, 2008). In practice, it can materialise as a low acceptance rate with repeated samples. The other caveat is that, even though calculating the solution of the mechanical system for each new sample takes almost the same computational effort no matter the number of employed parameters, one might require significantly more samples before the algorithm finds the high probability region with the additional parameters. One way to address this problem is to reduce the MHA sampling to manageable dimensions by approximating boundary conditions with basis functions, although the effect of that on the robustness of the algorithm must be considered first.

6.1. Finite Element Basis

A possible approach in reducing parameters’ dimension is to substitute the existing FE mesh on the boundary $\partial\Omega_{\text{MVE}}$ with a coarser one, using only some of the existing nodes. The initial MVE boundary mesh was constructed by assigning nodes at equal intervals with displacements interpolated from DNS, and every n -th node is then used for the boundary approximation, e.g. in Fig. 10a. For the clarity in visual presentation, the coordinates $\mathbf{X} \in \partial\Omega_{\text{MVE}}$, $X_1, X_2 \in [-2.5, 2.5]$ were transformed to $\xi(\mathbf{X}) \in \mathbb{R}$, $\xi \in [0, 20]$. For the approximation in the least squares sense, the displacement error of the boundary condition is:

$$\epsilon_{\text{rel}}^{\text{BC}} = \frac{\|\mathbf{u}_{\text{MVE}}^t(\mathbf{X}) - \mathbf{u}_{\text{DNS}}(\mathbf{X})\|_2}{\|\mathbf{u}_{\text{DNS}}(\mathbf{X})\|_2}, \quad \mathbf{X} \in \partial\Omega_{\text{MVE}}, \quad (28)$$

where $\mathbf{u}_{\text{MVE}}^t(\mathbf{X})$ is the boundary approximation with $2 \times t$ DOFs, $\mathbf{u}_{\text{DNS}}(\mathbf{X})$ is the exact boundary displacement obtained by the DNS. The error can be examined in Fig. 10b.



(a) Exact boundary conditions obtained by DNS, approx- (b) Relative displacement error at $\partial\Omega_{\text{MVE}}$ according to
 imated with a coarser mesh, tensile test. Eq. (28), depending on the number of DOFs.

Figure 10: (a) substitution with coarse mesh; (b) relative error of the boundary condition depending on the total number of employed degrees of freedom, FE basis.

To measure the effect of the approximation error, the material parameters are identified by the MHA with the fixed boundary conditions parameter λ_{kin} , where the exact boundary displacements were replaced with the approximation. As can be seen in Fig 11, the tensile test is generally more robust than the shear test in terms of the boundary error, as the results stop significantly deviating from the exact value for the number of employed nodes as little as 20% of the total, while in the shear test the material parameter K_2 continues to fluctuate for increasing t .

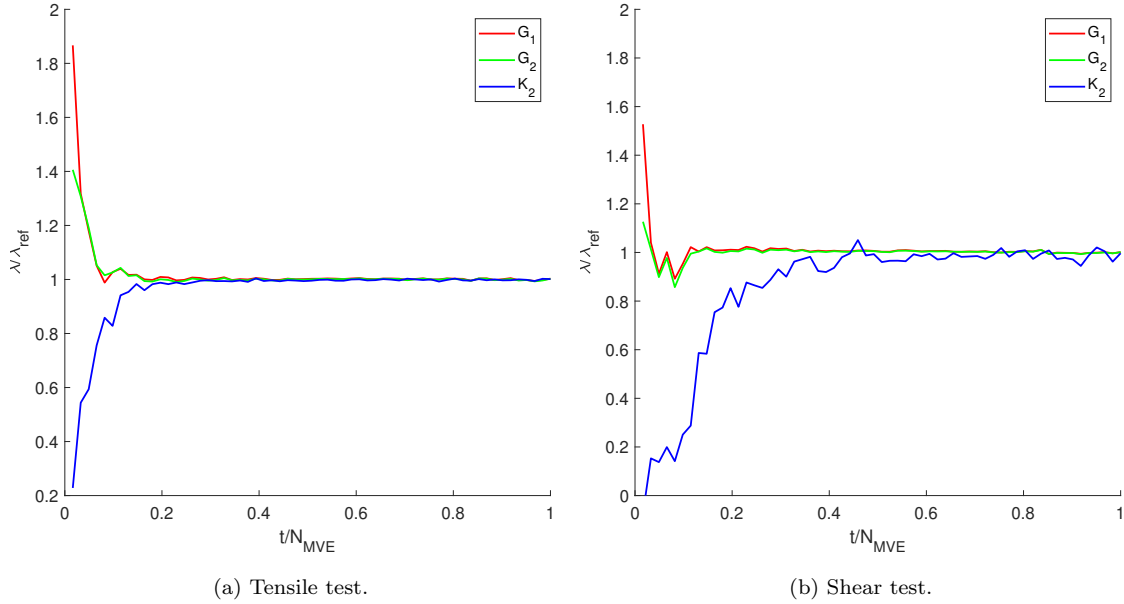


Figure 11: Identified results (means of the posterior distributions) for tensile (a) and shear (b) tests depending on the number of employed DOFs; boundary displacements are approximated with FE basis functions by the least squares method and fixed.

Now the boundary conditions parameter λ_{kin} can be added to MHA sampling. In Figs. 12 and 14 the experiment results are presented for tensile and shear test respectively. The number of total employed boundary DOFs was 2×61 (25%) and 2×244 (100%). To examine MHA's robustness in regards to the starting point of sampling, the first step of the algorithm was assumed with increasing σ of noise in the now sampled parameter λ_{kin} . For the test with the 244 nodes, the starting point for the material parameter λ_{mat} was in one experiment assumed as $0.9\lambda_{\text{ref},i}$, $i = 1, \dots, 4$ and in the other as the last accepted MHA sample from the experiment in Section 5.2. It should be noted that the first case was calculated only for $\sigma \in [0, 0.05]$ as the high kinematic fluctuations drastically increase computation time of the solvers. The walker's step size in the boundary conditions parameter's dimensions $\sigma_{q,\text{kin}}$ is scaled proportionally to $\sigma \max_{\mathbf{Y} \in \Omega_{\text{MVE}}} (\|\mathbf{u}_{\text{DNS}}(\mathbf{Y})\|_2)$.

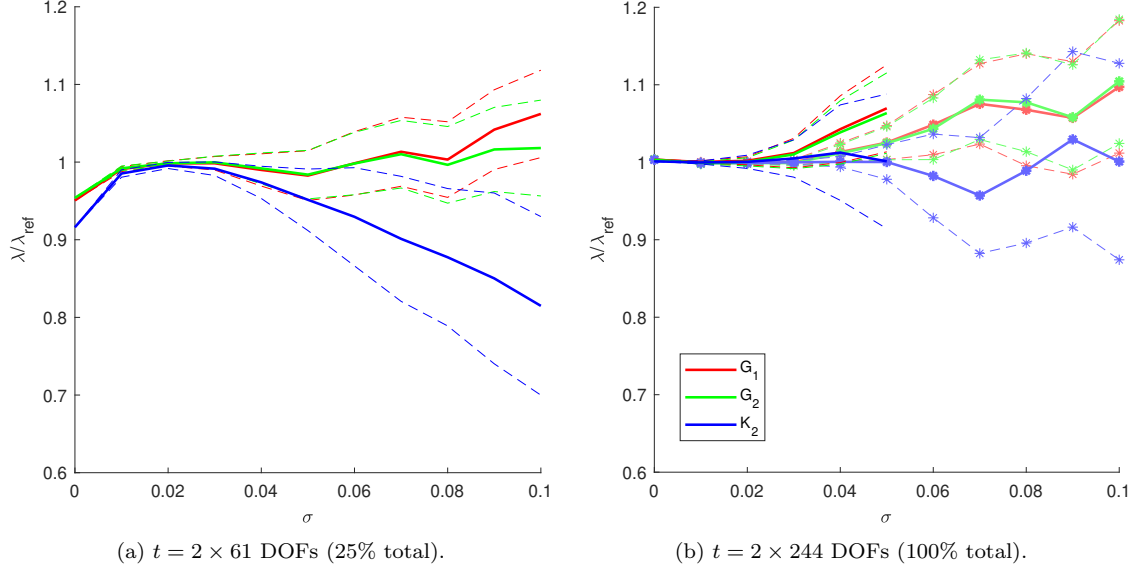


Figure 12: Identified parameters for different number of employed DOFs, mean (solid) \pm standard deviation (dashed), increasing $\sigma \in [0, 0.1]$, $N = 16\,000$ steps of MHA, tensile test, (*) denotes the experiment with the starting point as the last accepted sample of each MC iteration for a given σ from the MHA with fixed boundary experiment in Section 5.2.

In the tensile test with 2×244 DOFs, the robustness was increased significantly for $\sigma \in [0, 0.5]$ compared to IDIC and MHA with fixed boundary, especially when the starting point was assumed from the last sample of the fixed boundary experiment (Fig. 12). Essentially, we can look at this experiment as if the MHA walker started with fixed boundary conditions and then after reaching the high probability region λ_{kin} was relaxed. In the experiment with reduced number of degrees of freedom, while the robustness was increased for small σ , the error-causing effect of kinematic smoothing is obvious, particularly for λ_{K2} .

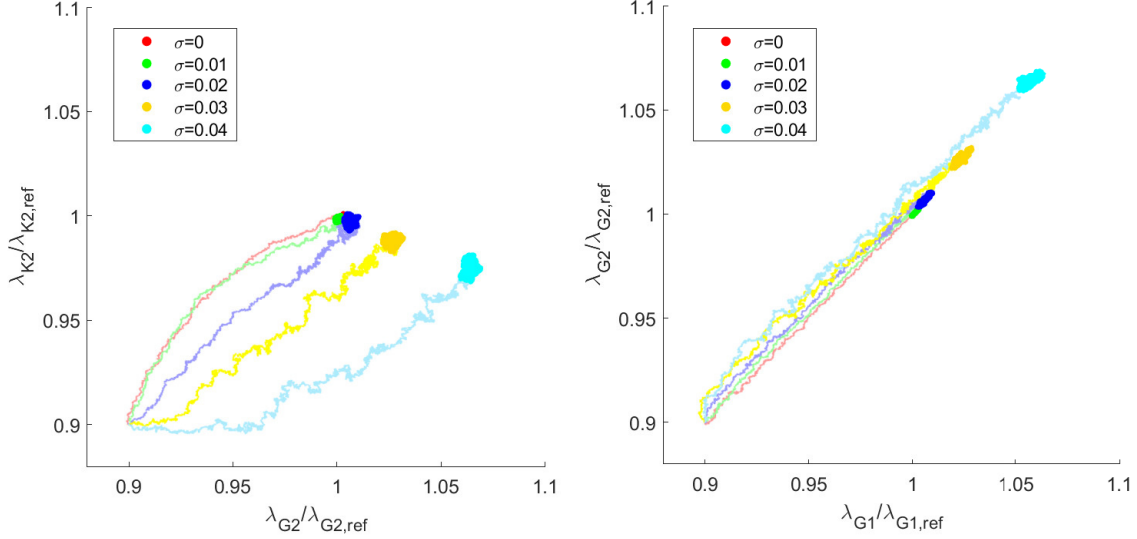


Figure 13: 2D projection of MHA sampling in material parameter dimensions, fibre shear modulus G_2 and bulk modulus K_2 (left), matrix shear modulus G_1 and fibre shear modulus G_2 (right); number of DOFs $t = 2 \times 244$ (100%), single MC iteration, increasing $\sigma \in [0, 0.04]$, $N = 16\,000$ steps of MHA, tensile test.

Some of the MHA walks for one of the MC realisations is shown in Fig. 13. From there on, the burned in samples are shown in pale colours. The walks show a strong linear relationship between λ_{G_1} and λ_{G_2} , from which the contrast constant ϱ can be deduced. The resulting posterior probability functions can be inspected in the Appendix in Figs. 28, 30. The high probability regions were also significantly expanded compared to the fixed boundary experiment (shown as $\sigma = 0$, red).

The shear test experiment is shown in Fig. 14. From the walks for the 2×244 DOFs experiment in Fig. 15, it seems like the error in the inclusion shear modulus λ_{G_2} is causing radical direction change along the bulk modulus λ_{K_2} , somewhat similar, but less dramatic effect was also present in the tensile test. While in the shear test with the reduced number of nodes identified values are seemingly closer to the reference value, the algorithm has not yet converged in the high probability region (see Fig. 32 in the Appendix).

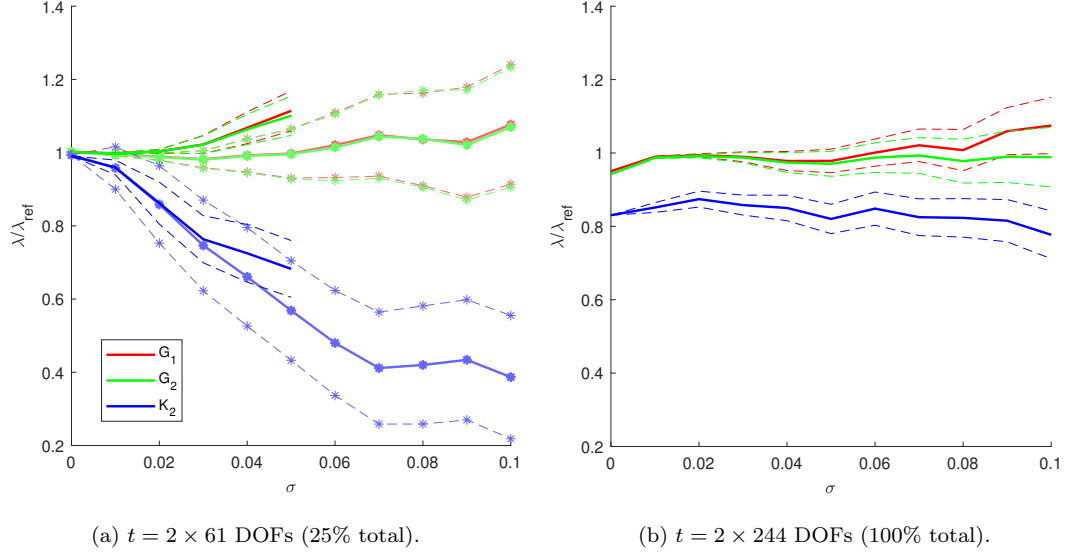


Figure 14: Identified parameters for different number of employed DOFs, mean (solid) \pm standard deviation (dashed), increasing $\sigma \in [0, 0.1]$, $N = 16\,000$ steps of MHA, shear test, (*) denotes the experiment with the starting point is the last accepted sample of each MC iteration for a given σ from the MHA with fixed boundary experiment in Section 5.2.

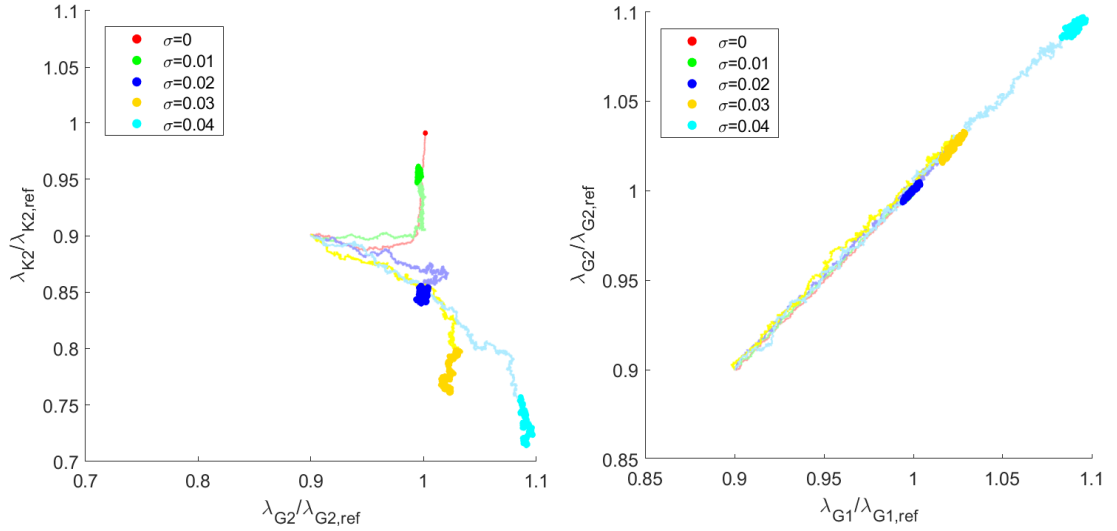


Figure 15: 2D projection of MHA sampling in material parameter dimensions, fibre shear modulus G_2 and bulk modulus K_2 (left), matrix shear modulus G_1 and fibre shear modulus G_2 (right); number of DOFs $t = 2 \times 244$ (100%), single MC iteration, increasing $\sigma \in [0, 0.04]$, $N = 16\,000$ steps of MHA, shear test.

The progress of the relative boundary condition error during MHA sampling for different starting noise $\sigma = [0, 0.1]$ is shown in Fig. 16. In both shear and tensile test the error decreases throughout MHA run for the value of σ up to 0.08, which suggests the possibility of the algorithm converging in the high-probability region close to the reference value after many more additional iterations. On the other hand, for high values of σ , the error is steadily increasing.

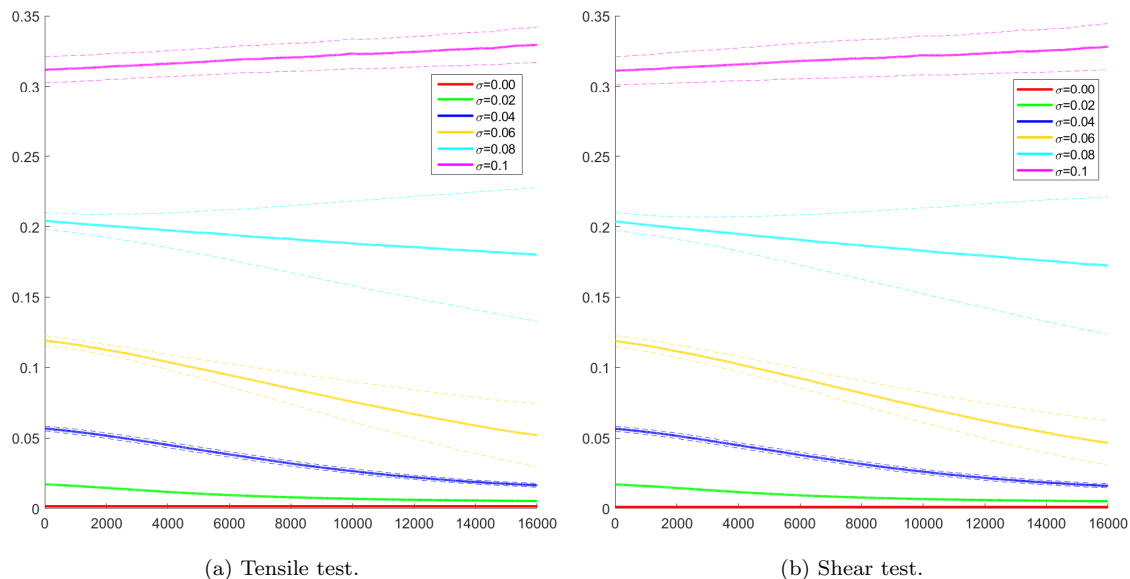


Figure 16: Average error in the boundary conditions for $\sigma \in [0, 0.1]$, MHA sampling $t = 2 \times 244$ (100%), FE basis, 55 MC iterations, the starting point of MHA is the last accepted sample of each MC iteration for a given σ from the MHA with fixed boundary experiment in Subsection 5.2.

6.2. Comparison of MHA to BE-IDIC

One would be interested, of course, in how MHA with relaxed boundary compares to the existing BE-IDIC algorithm that also incorporates boundary conditions parameters. The robustness test in regards to the boundary noise was conducted for BE-IDIC, where the identified parameter λ_{kin} was the same as in Section 6.1. The results are shown in Fig. 17.

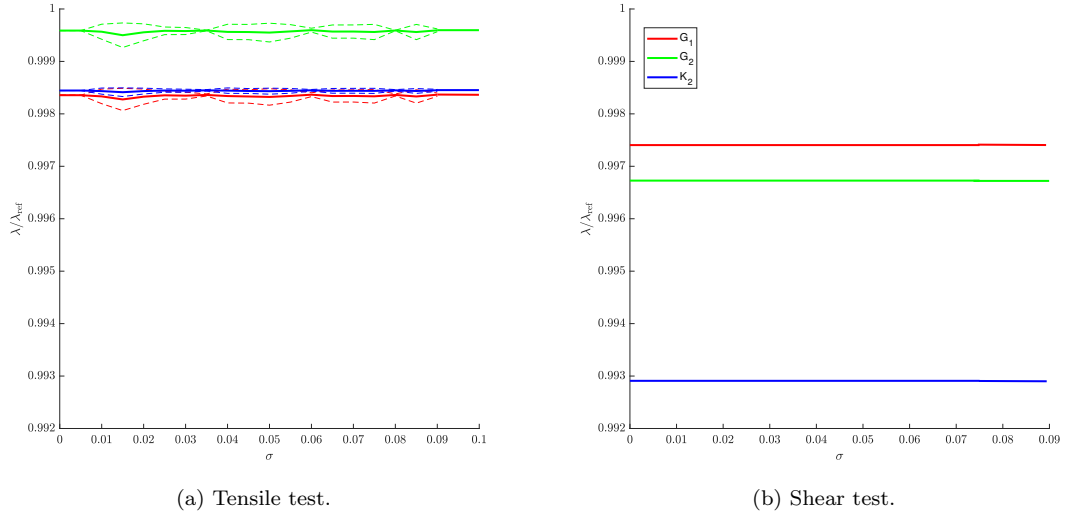


Figure 17: Robustness test for BE-IDIC algorithm analogous to MHA experiment in Section 5.2, increasing noise $\sigma = [0, 0.1]$ in initial boundary conditions, material parameter identification for tensile (a) and shear (b) tests, mean (solid) \pm standard deviation (dashed).

The BE-IDIC algorithm converges to the same value, regardless of the starting point. The variation in the tensile test is due rounding errors. Even though the end result is very close to the reference value, the method does not provide much information beyond that.

As was shown in the previous sections, MHA algorithm is not very effective in reaching the supposed high-probability region when the starting point is not sufficiently close to the reference value of the parameter. Nevertheless, the MHA algorithm can be used to enrich the identification data after a deterministic algorithm (like BE-IDIC) converged in the high-probability region.

Let us consider the following experiment: MHA is run with the starting point provided by BE-IDIC, normalisation parameter λ_{K1} is relaxed in addition to all available boundary conditions DOFs employed (FE basis). The $N = 32\,000$ step sampling and resulting posterior probability distributions are shown in Figs. 18-23. The strongest linear relation is suggested between the individual parameters of matrix shear modulus G_1 and fibre shear modulus G_2 in both tensile and shear test (Figs. 19, 22). The possible reason behind lesser robustness of the shear test might be the inability to establish a correct ratio between the parameters other than G_1 and G_2 .

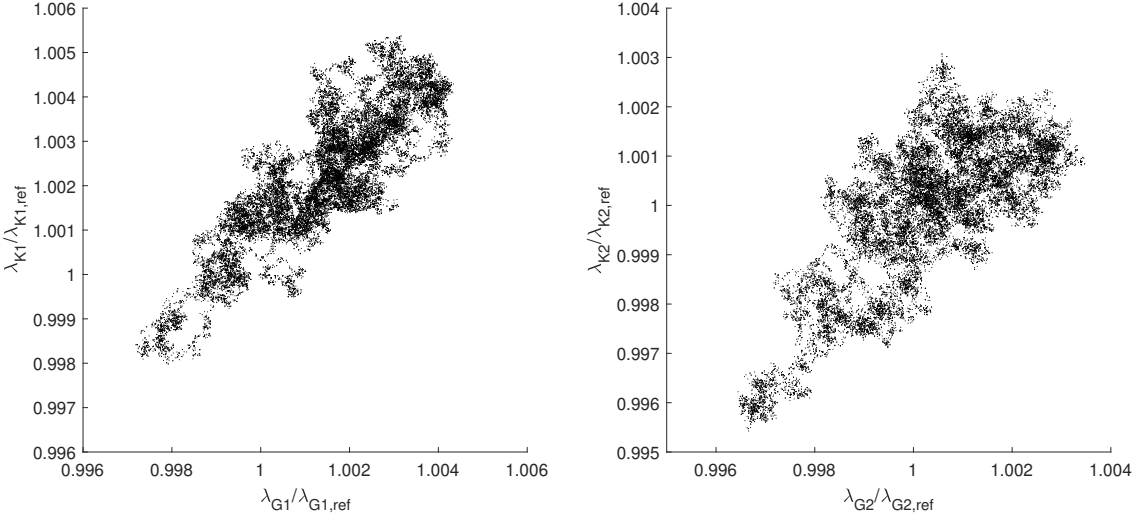


Figure 18: 2D projections of MHA sampling in material parameter dimensions, matrix shear modulus G_1 and matrix bulk modulus K_1 (left), fibre shear modulus G_2 and fibre bulk modulus K_2 (right); number of DOFs $t = 2 \times 244$ (100%), $N = 32\,000$ steps of MHA, starting point provided by BE-IDIC, tensile test.

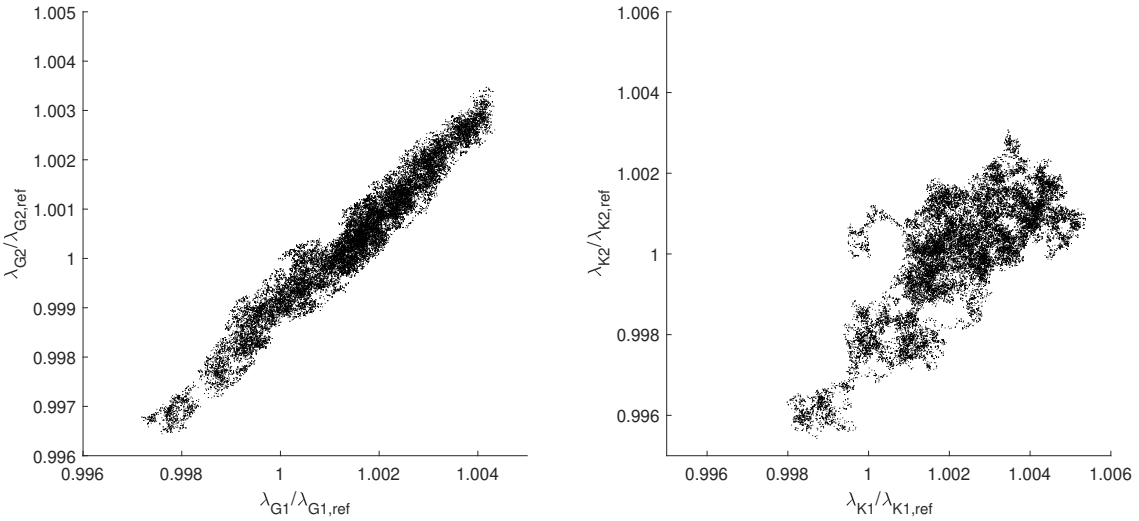


Figure 19: 2D projections of MHA sampling in material parameter dimensions, matrix shear modulus G_1 and fibre shear modulus G_2 (left), matrix bulk modulus K_1 and fibre bulk modulus K_2 (right); number of DOFs $t = 2 \times 244$ (100%), $N = 32\,000$ steps of MHA, starting point provided by BE-IDIC, tensile test.

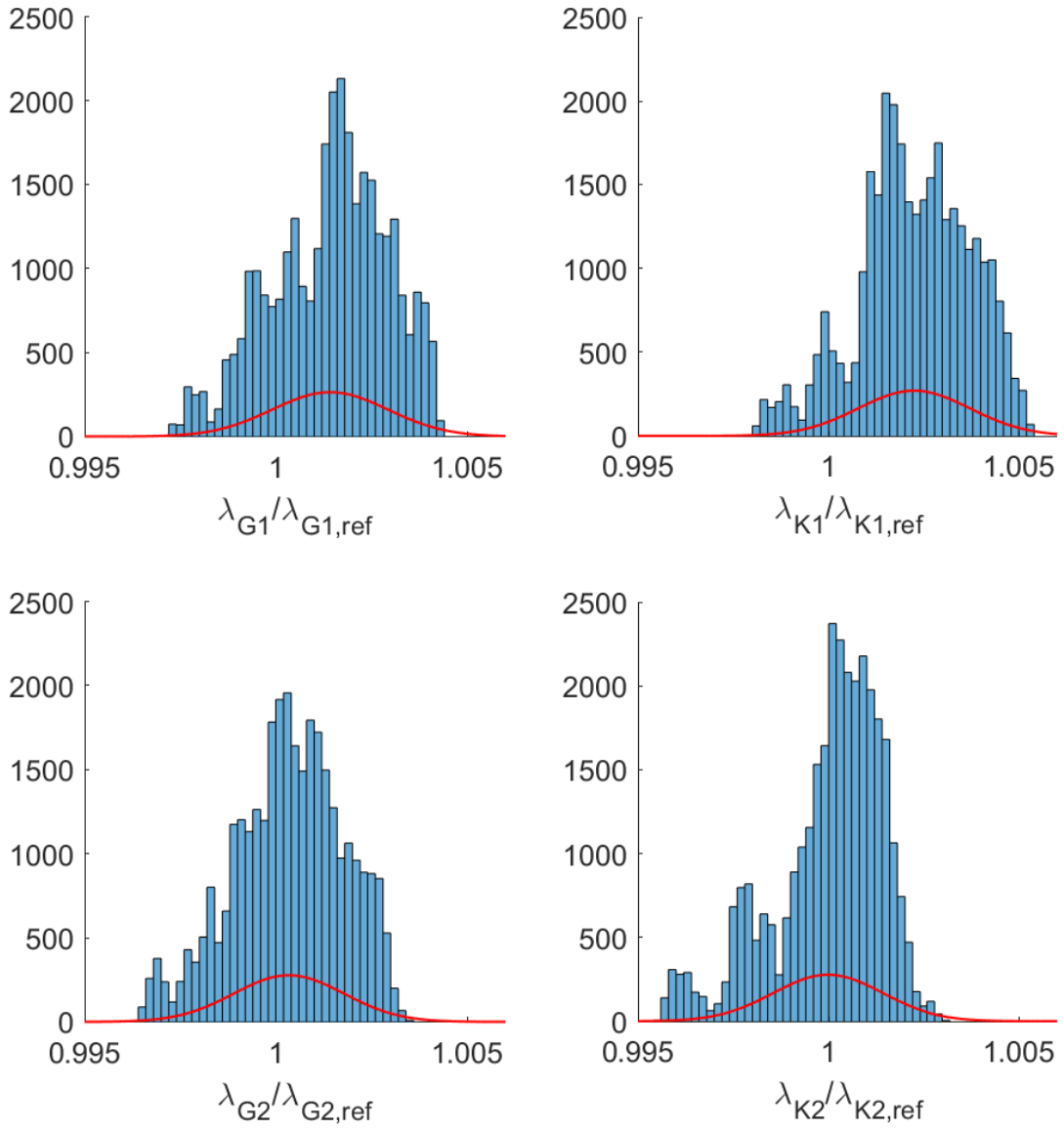


Figure 20: Histograms and approximated posterior PDFs for individual material parameters, $N = 32\,000$ steps of MHA, number of DOFs $t = 2 \times 244$ (100%), starting point provided by BE-IDIC, tensile test.

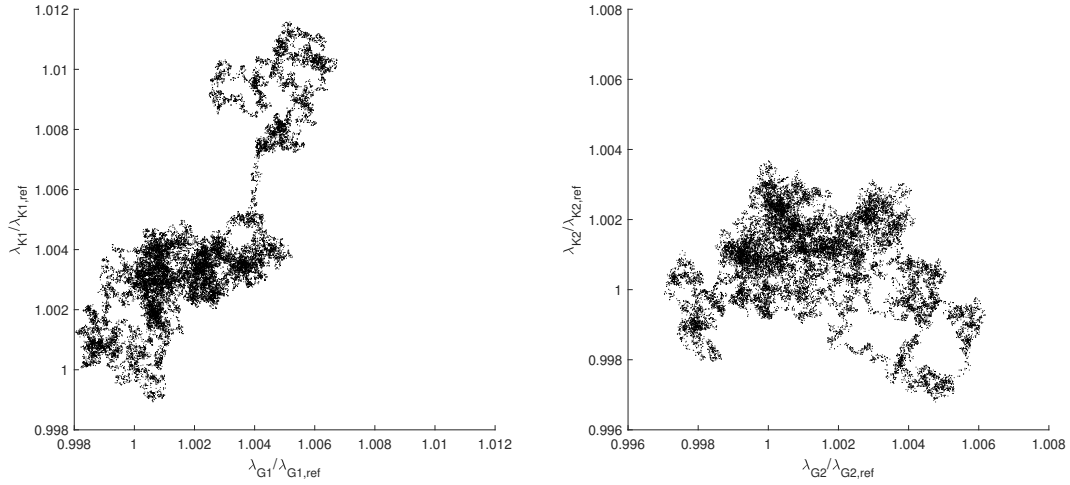


Figure 21: 2D projections of MHA sampling in material parameter dimensions, matrix shear modulus G_1 and matrix bulk modulus K_1 (left), fibre shear modulus G_2 and fibre bulk modulus K_2 (right); number of DOFs $t = 2 \times 244$ (100%), $N = 32\,000$ steps of MHA, starting point provided by BE-IDIC, shear test.

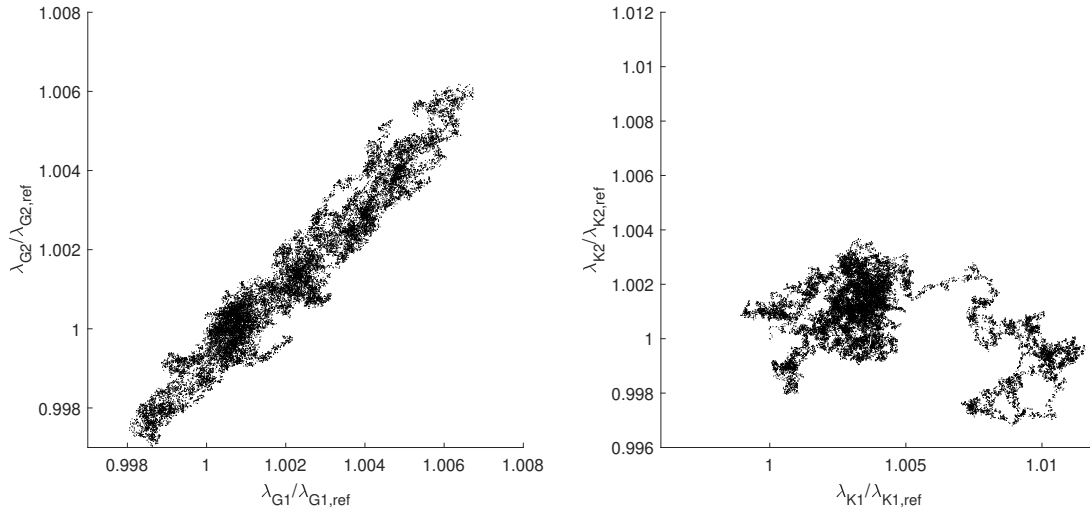


Figure 22: 2D projections of MHA sampling in material parameter dimensions, matrix shear modulus G_1 and fibre shear modulus G_2 (left), matrix bulk modulus K_1 and fibre bulk modulus K_2 (right); number of DOFs $t = 2 \times 244$ (100%), $N = 32\,000$ steps of MHA, starting point provided by BE-IDIC, shear test.

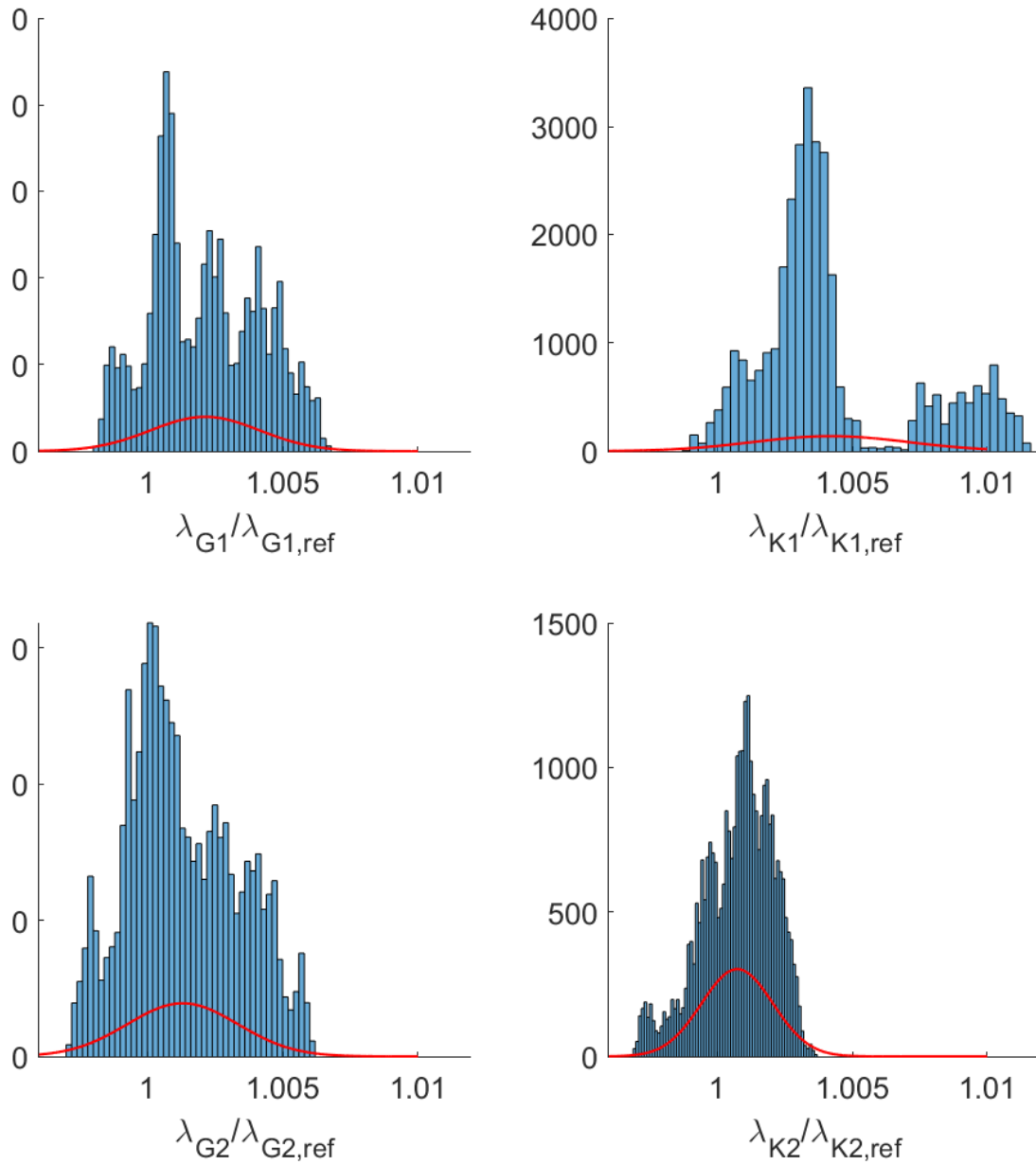


Figure 23: Histograms and approximated posterior PDFs for individual material parameters, $N = 32\,000$ steps of MHA, number of DOFs $t = 2 \times 244$ (100%), starting point provided by BE-IDIC, shear test.

Note also the two distinct clusters in the matrix bulk modulus K_1 (see Fig. 23),

the parameter that was previously fixed. As the Dirichlet boundary conditions due to the reasons discussed before only allow the parameter ratios to be established, so a certain “drift” is expected. Curiously, its effects are stronger for the fibre parameters in the shear test compared to the tensile test. Overall, the shift is happening toward the higher values, so the material is identified to be somewhat stiffer than in reality.

The results for both tensile and shear test are presented in Tab. 2, where the value obtained by the BE-IDIC is compared to the mean \pm standard deviation and the 2.5%–97.5% quantile of the posterior distribution provided by MHA.

	Ref.	BE-IDIC (t)	MHA (t)	BE-IDIC (s)	MHA (s)
G_1	1	0.9984	1.0014 ± 0.0015 95% $\in [0.9981, 1.004]$	0.9974	1.0021 ± 0.002 95% $\in [0.9986, 1.0059]$
K_1	3	3 (fixed)	3.0067 ± 0.0044 95% $\in [2.9967, 3.0143]$	3 (fixed)	3.0126 ± 0.0086 95% $\in [3.0005, 3.0320]$
G_2	4	3.9984	4.0013 ± 0.0058 95% $\in [3.9883, 4.0112]$	3.9868	4.0052 ± 0.0082 95% $\in [3.9910, 4.0219]$
K_2	12	11.9808	11.9998 ± 0.0173 95% $\in [11.9549, 12.0245]$	11.9148	12.0090 ± 0.0159 95% $\in [11.9705, 12.0343]$
ϱ	4	3.9992	3.9933 ± 0.0022 95% $\in [3.9894, 3.9977]$	3.9844	3.9915 ± 0.0071 95% $\in [3.9756, 4.0007]$

Table 2: Comparison of the parameter identification results for MHA and BE-IDIC, (t) stands for tensile test, (s) stands for shear test.

6.3. Parametrisation of the Noise Present in Applied Kinematic Boundary Conditions

As shown in the previous subsections, kinematic field smoothing has a negative effect on the material parameter identification, so one would be interested in reducing the number of sampled parameters without losing the heterogeneity of the boundary. As the boundary $\partial\Omega_{\text{MVE}}$ burdened with random noise can be looked at as an unknown parameter field, we can try to parametrise it based on the random field theory (Havelka et al., 2019). We assume a random field $a(\mathbf{X})$, $\mathbf{X} \in \partial\Omega_{\text{MVE}}$, a stochastic process in space. Then we can state the parametrisation problem as follows (Xiu, 2010): let $(Y_t, t \in T)$ be a stochastic process of the random inputs, where the index t belongs to an index set T , and find a suitable transformation function R such that $Y_t \approx R(Z)$, where $Z = (Z_1, \dots, Z_d)$, $d \geq 1$, are mutually independent random variables. As the index set T is infinite-dimensional domain and d is a finite integer, the transformation is only approximate. To consider the finite-dimensional

version of Y_t we first discretise the index domain T into a set of finite indices and then study the process

$$(Y_{t_1}, \dots, Y_{t_n}), \quad t_1, \dots, t_n \in T,$$

which is now a finite-dimensional random vector. To reduce the dimensionality of the random process we introduce a parameter vector into the model by applying the truncated Karhunen–Loève expansion (KLE). Let $\boldsymbol{\mu}_Y(t)$ be the mean of the input process $Y_t(\boldsymbol{\omega}) = a(\mathbf{X})$, $\mathbf{X} = \mathbf{X}(t)$ is a parametrisation of the boundary $\partial\Omega_{\text{MVE}}$, where $t \in T \subset \mathbb{R}$, T is an interval. Let $C(t, s) = \text{cov}(Y_t, Y_s)$ be its covariance function. The Karhunen–Loève expansion of Y_t is given by:

$$Y_t(\boldsymbol{\omega}) \approx \mu_Y(t) + \sum_{i=1}^d \sqrt{\lambda_i} \psi_i(t) Y_i(\boldsymbol{\omega}), \quad d \geq 1, \quad (29)$$

where ψ_i are the orthogonal eigenfunctions and λ_i are the corresponding eigenvalues of the eigenvalue problem

$$\int_T C(t, s) \psi_i(s) ds = \lambda_i \psi_i(t), \quad t, s \in T \quad (30)$$

and $Y_i(\boldsymbol{\omega})$ are mutually uncorrelated random variables satisfying

$$\mathbb{E}[Y_i] = 0, \quad \mathbb{E}[Y_i Y_j] = \delta_{ij}$$

where δ_{ij} is Kronecker's delta and defined by

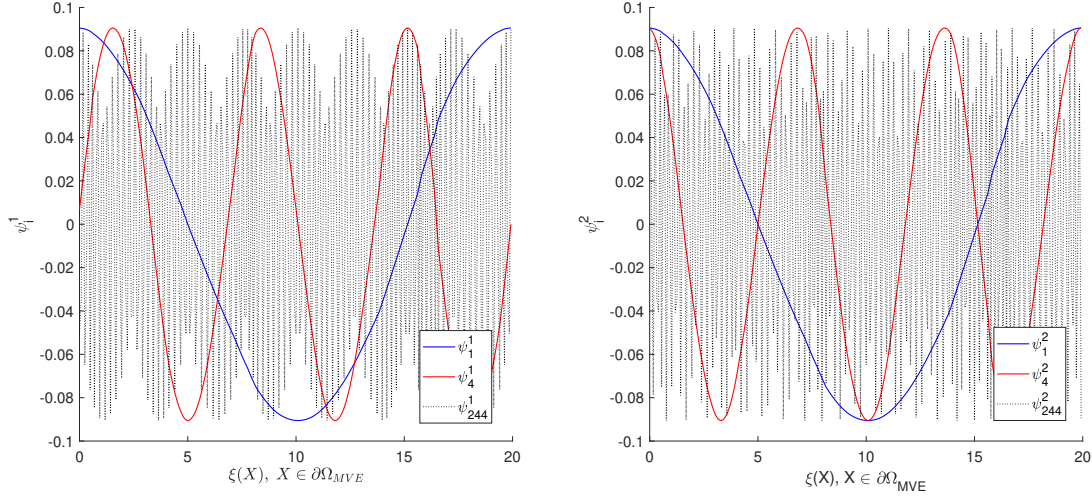
$$Y_i(\boldsymbol{\omega}) = \frac{1}{\sqrt{\lambda_i}} \int_T (Y_t(\boldsymbol{\omega}) - \mu_Y(t)) \psi_i(t) dt, \quad i = 1, \dots, d.$$

For our particular problem, to set the covariance functions $C_1(t, s)$ and $C_2(t, s)$ for displacements in X_1 and X_2 , one can use the boundary data obtained by DNS:

$$C_1(t, s) = \frac{\mathbf{u}_1(\mathbf{X}(t)) \cdot \mathbf{u}_1(\mathbf{X}(s))}{\|\mathbf{u}_1\|_2}, \quad t, s \in T, \quad (31)$$

$$C_2(t, s) = \frac{\mathbf{u}_2(\mathbf{X}(t)) \cdot \mathbf{u}_2(\mathbf{X}(s))}{\|\mathbf{u}_2\|_2}, \quad t, s \in T, \quad (32)$$

where $\mathbf{u}_1 = [\mathbf{u}_1^1, \dots, \mathbf{u}_{n_u/2}^1]^\top \in \mathbb{R}^{n_u}$, $\mathbf{u}_2 = [\mathbf{u}_1^2, \dots, \mathbf{u}_{n_u/2}^2]^\top \in \mathbb{R}^{n_u}$ are nodal displacements on the boundary $\partial\Omega_{\text{MVE}}$ in X_1 and X_2 directions. Some of the resulting basis functions are illustrated in Fig. 24.



(a) KLE eigenvectors (basis functions) for displacements along X_1 . (b) KLE eigenvectors (basis functions) for displacements along X_2 .

Figure 24: Some KLE eigenvectors (basis functions).

Let us suppose that we have obtained boundary conditions data burdened with noise, cf. Eq. (26). Even though describing boundary conditions with perfect accuracy is not our main concern, “purifying” the data will lead to more accurate identification of material parameters. A way to do that would be fitting the noise in the boundary conditions in the least square sense with a number of basis functions obtained by the KLE from Eq. (29). The relative error of the resulting boundary is then:

$$\epsilon_{rel}^{BC} = \frac{\|\mathbf{u}_{MVE}(\mathbf{X}(t)) - \Psi_n \mathbf{c}_n - \mathbf{u}_{DNS}(\mathbf{X}(t))\|}{\|\mathbf{u}_{MVE}(\mathbf{X}(t)) - \mathbf{u}_{DNS}(\mathbf{X}(t))\|}, \quad t \in T, \quad (33)$$

where Ψ_n is the $n \times N_{MVE}$ matrix of eigenvectors ψ_i in Eq. (29), N_{MVE} is the number of data points along $\partial\Omega_{MVE}$, $\mathbf{c}_n = [c^1, \dots, c^n]^T$ is the coefficients obtained by approximating the superimposed noise with the least squares method.

As we can see in Fig. 25, the relationship between the number of basis functions (chosen in the ascending order of the respective eigenvalues) used and the relative error is not linear, e.g. to reduce the error by 50%, approximately 75% of the total number of available KLE basis functions must be used. To quantify the effect of the noise smoothing in the boundary conditions in the fixed boundary test, the KLE approximation of noise is subtracted from the boundary conditions (Figs. 34, 35 in the Appendix). The tests were performed for $N = 4\,000$ MHA steps. For the number of employed KLE functions equal to 2×61 (out of total 2×244) and $\sigma = 0.1$, the

reduction in the error in the mean was about 50% for the parameters G_1 and G_2 , and 80% for the K_2 , while the standard deviation was reduced by nearly 50% for G_1 and G_2 and more than 66% for K_2 . The L^2 error of the boundary conditions was reduced by only about 10%. The error is also reduced considerably for the shear test with the exception of the K_2 parameter. As was mentioned before, the results above are hypothetical, because the boundary conditions noise is unknown and random, but they should represent the end result after many MHA iterations, assuming, of course, that the algorithm cannot converge to a "better" minimum of \mathcal{R}_{MHA} , hence a different fit to the noise from the fit in a least squares sense.

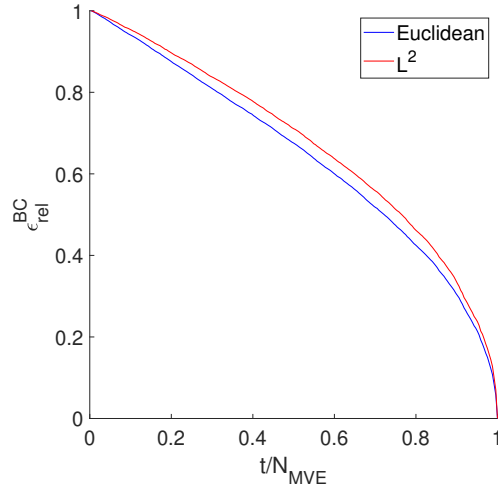
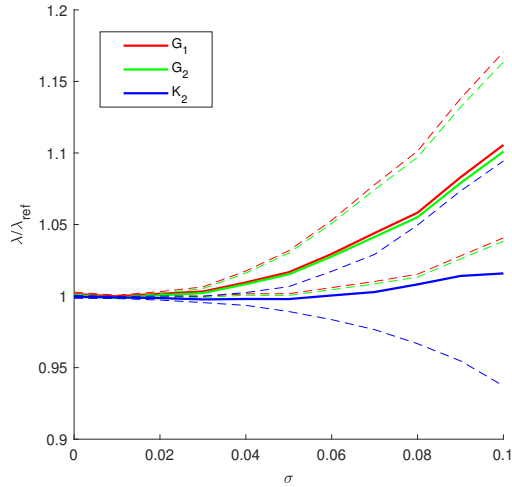


Figure 25: Relative displacement error at $\partial\Omega_{MVE}$ according to Eq. (33), depending on the number of employed KLE basis functions.

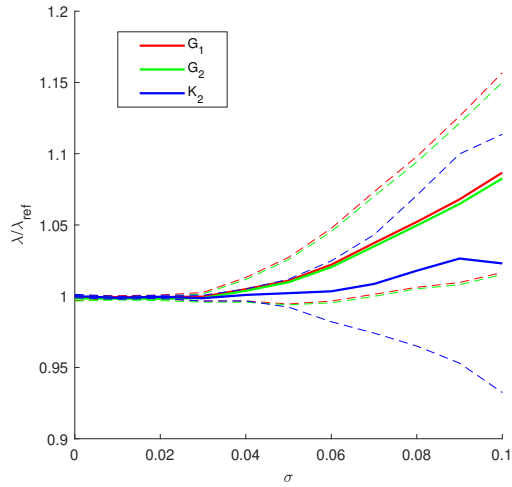
Let us now move on to adding degrees of freedom to the MHA algorithm, so that the boundary conditions can be written in the form:

$$\mathbf{u}_{MVE}(\mathbf{X}, \hat{\boldsymbol{\zeta}}_t) = \mathbf{u}_{DNS}(\mathbf{X}) + \sigma \max_{\mathbf{Y} \in \Omega_{MVE}} (\|\mathbf{u}_{DNS}(\mathbf{Y})\|_2) \boldsymbol{\mu} - \Psi_t \hat{\boldsymbol{\zeta}}_t, \quad \mathbf{X} \in \partial\Omega_{MVE}, \quad (34)$$

where noise parameter $\hat{\boldsymbol{\zeta}}_t \in \mathbb{R}^t$ is now substituting $\boldsymbol{\lambda}_{kin}$ as the boundary conditions parameter. As it proved a somewhat more effective strategy before, the last accepted sample of each MC iteration for a given σ from the fixed boundary experiment is assumed as the starting point of the MHA algorithm. The results for the number of the employed KL functions equal to 2×61 (25%) and 2×244 (100%), $N = 16\,000$ steps and burn-in $N_0 = 0.75N$ are shown in Figs. 26, 27.

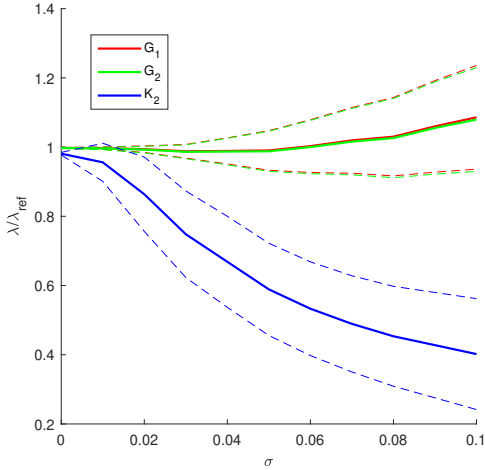


(a) $t = 2 \times 61$ KLE basis functions (25% total).

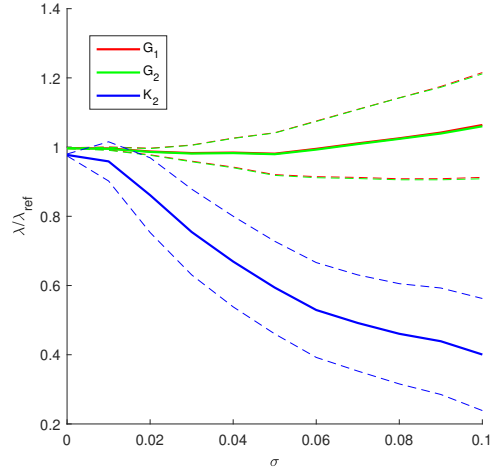


(b) $t = 2 \times 244$ KLE basis functions (100% total).

Figure 26: Identified parameters for different number of employed KLE basis functions, mean (solid) \pm standard deviation (dashed), increasing $\sigma \in [0, 0.1]$, $N = 16\,000$ steps of MHA, tensile test, the starting point of MHA is the last accepted sample of each MC iteration for a given σ from the MHA with fixed boundary experiment in Section 5.2.



(a) $t = 2 \times 61$ KLE basis functions (100% total).



(b) $t = 2 \times 244$ KLE basis functions (25% total).

Figure 27: Identified parameters for different number of employed KLE basis functions, mean (solid) \pm standard deviation (dashed), increasing $\sigma \in [0, 0.1]$, $N = 16\,000$ steps of MHA, shear test, the starting point of MHA is the last accepted sample of each MC iteration for a given σ from the MHA with fixed boundary experiment in Section 5.2.

The sampling step size $\sigma_{q,\text{kin}}$ was again adjusted relative to σ of noise. We can

see that in the tensile test for $\sigma \leq 0.03$, the algorithm converged very close to the precise values of λ and then starts deviating with a slight improvement over the fixed boundary conditions. The effect, however, was not observed for either number of functions in the shear test.

7. Summary and Conclusions

In this contribution, a study comparing the robustness of Metropolis-Hastings algorithm (MHA) to deterministic Integrated Digital Image Correlation (IDIC) and Boundary Enriched Integrated Digital Image Correlation (BE-IDIC) has been presented. To this end, heterogeneous specimen with a random microstructure have been subjected to two virtual mechanical tests under plane strain conditions, one to primarily introduce tension, the other to introduce shear. The experiments have shown a similar behaviour of MHA with fixed boundary conditions to IDIC for both the systematic error and random error in the boundary conditions.

Two possible ways of reducing the dimension of the boundary conditions parameter were suggested: a) substituting the employed discretisation mesh on the boundary with a coarser one; b) approximating the random boundary error as an unknown parameter field by truncated Karhunen–Loève expansion. The robustness test for random error in the boundary conditions did not suggest any benefit in reducing dimensionality in the employed configuration. Both a) and b) methods performed well for small noise, for higher values either has converged to the probability region more akin to the fixed boundary test, suggesting that the boundary conditions parameter λ_{kin} does not converge fast enough for the material parameter λ_{mat} to stop compensating the error. The a) method also caused ill-conditioned mechanical systems for high starting noise more often than b) method.

In total, MHA with relaxed boundary conditions proved to be less efficient and more computationally costly than BE-IDIC in finding the high probability region. Its benefits, however, are:

- adding degrees of freedom does not increase computational cost and memory requirements;
- it provides more statistical data;
- one can use the results of the deterministic methods to improve upon;
- it does not require a normalisation parameter to be fixed at the exact reference value.

It is important to note that the virtual test employed an exact constitutive model that is not likely reproducible in real experiments, and that also other significant sources of errors exist and must be accounted for. Thus, stochastic approach might be applicable to fine-tuning the sensitivity analyses to various other sources of errors and tests on real experiments. Suitability for ill-posed problems should be further investigated.

References

- Au, S.K., Beck, J.L., 2001. Estimation of small failure probabilities in high dimensions by subset simulation. *Probabilistic Engineering Mechanics* 16, 263–277.
- Avril, S., Bonnet, M., Caro-Bretelle, A., Grédiac, M., Hild, F., Ienny, P., Latourte, F., Lemosse, D., Pagano, S., Pagnacco, E., Pierron, F., 2008. Overview of identification methods of mechanical parameters based on full-field measurements. *Experimental Mechanics* 48. doi:[10.1007/s11340-008-9148-y](https://doi.org/10.1007/s11340-008-9148-y).
- Blaheta, R., Béréš, M., Domesová, S., Pan, P., 2018. A comparison of deterministic and Bayesian inverse with application in micromechanics. *Applications of Mathematics* 63, 665–686. doi:[10.21136/AM.2018.0195-18](https://doi.org/10.21136/AM.2018.0195-18).
- Bornert, M., Brémand, F., Doumalin, P., Dupré, J.C., Fazzini, M., Grédiac, M., Hild, F., Mistou, S., Molimard, J., Orteu, J.J., Robert, L., Surrel, Y., Vacher, P., Wattrisse, B., 2009. Assessment of digital image correlation measurement errors: Methodology and results. *Experimental Mechanics* 49, 353–370. doi:[10.1007/s11340-008-9204-7](https://doi.org/10.1007/s11340-008-9204-7).
- Evans, L.C., 2010. *Partial Differential Equations*. 2 ed., American Mathematical Society Providence, Rhode Island.
- Geuzaine, C., Remacle, J.F., 2009. Gmsh: a three-dimensional finite element mesh generator with built-in pre- and post-processing facilities. *International Journal for Numerical Methods in Engineering* 79, 1309–1331.
- Havelka, J., Kučerová, A., Sýkora, J., 2019. Dimensionality reduction in thermal tomography. *Computers and Mathematics with Applications* 78, 3077–3089. doi:[10.1016/j.camwa.2019.04.019](https://doi.org/10.1016/j.camwa.2019.04.019). *Applications of Partial Differential Equations in Science and Engineering*.
- Janouchová, E., Kučerová, A., 2018. Bayesian inference of heterogeneous viscoplastic material parameters. *Acta Polytechnica CTU Proceedings* 15, 41–45. doi:[10.14311/APP.2018.15.0041](https://doi.org/10.14311/APP.2018.15.0041).

- Jones, E., Iadicola, M., 2018. A Good Practices Guide for Digital Image Correlation. International Digital Image Correlation Society. doi:[10.32720/idics/gpg.ed1](https://doi.org/10.32720/idics/gpg.ed1).
- Katafygiotis, L., Zuev, K., 2008. Geometric insight into the challenges of solving high-dimensional reliability problems. Probabilistic Engineering Mechanics 23, 208–218. doi:[10.1016/j.pro bengmech.2007.12.026](https://doi.org/10.1016/j.pro bengmech.2007.12.026).
- Leclerc, H., Périé, J., Roux, S., Hild, F., 2009. Integrated digital image correlation for the identification of mechanical properties. Computer Vision/Computer Graphics Collaboration Techniques 5496, 161–171. doi:[10.1007/978-3-642-01811-4_15](https://doi.org/10.1007/978-3-642-01811-4_15).
- Lee, P.M., 2012. Bayesian Statistics: An Introduction. 4 ed., Wiley.
- MathWorks Inc., 2018. MATLAB R2018a for Windows 64-bit.
- Neggens, J., Hoefnagels, J., Hild, F., Roux, S., Geers, M., 2014. Direct stress-strain measurements from bulged membranes using topography image correlation. Experimental Mechanics 54, 717–727. doi:[10.1007/s11340-013-9832-4](https://doi.org/10.1007/s11340-013-9832-4).
- Oberkampf, W.L., DeLand, S.M., Rutherford, B.M., Diegert, K.V., Alvin, K.F., 2002. Error and uncertainty in modeling and simulation. Reliability Engineering and System Safety 75, 333–357. doi:[10.1016/S0951-8320\(01\)00120-X](https://doi.org/10.1016/S0951-8320(01)00120-X).
- Rokoš, O., Hoefnagels, J., Peerlings, R., Geers, M., 2018. On micromechanical parameter identification with integrated DIC and the role of accuracy in kinematic boundary conditions. International Journal of Solids and Structures 146, 241–259. doi:[10.1016/j.ijsolstr.2018.04.004](https://doi.org/10.1016/j.ijsolstr.2018.04.004).
- Roux, S., Hild, F., 2006. Stress intensity factor measurements from digital image correlation: post-processing and integrated approaches. International Journal of Fracture 140, 141–157. doi:[10.1007/s10704-006-6631-2](https://doi.org/10.1007/s10704-006-6631-2).
- Ruybalid, A., Hoefnagels, J., van der Sluis, O., Geers, M., 2017. Image-based interface characterization with a restricted microscopic field of view. International Journal of Solids and Structures 132-133, 218–231. doi:[10.1016/j.ijsolstr.2017.08.020](https://doi.org/10.1016/j.ijsolstr.2017.08.020).
- Shakoor, M., Buljac, A., Neggens, J., Hild, F., Morgeneyer, T.F., Helfen, L., Bernacki, M., Bouchard, P.O., 2017. On the choice of boundary conditions for micromechanical simulations based on 3d imaging. International Journal of Solids and Structures 112, 83–96. doi:[10.1016/j.ijsolstr.2017.02.018](https://doi.org/10.1016/j.ijsolstr.2017.02.018).

- Stuart, A., Ord, J., 1994. Kendall's Advanced Theory of Statistics. volume 1. Hodder Arnold.
- Tadmor, E.B., Miller, E.R., Elliott, R.S., 2012. Continuum Mechanics and Thermodynamics: From Fundamental Concepts to Governing Equations. Cambridge University Press.
- Viggiani, G., Hall, S.A., 2008. Full-field measurements, a new tool for laboratory experimental Geomechanics. IOS Press.
- Xiu, D., 2010. Numerical Methods for Stochastic Computations: A Spectral Method Approach. Princeton University Press.

8. Appendix

This section provides extended results of the experiments described in the main body.

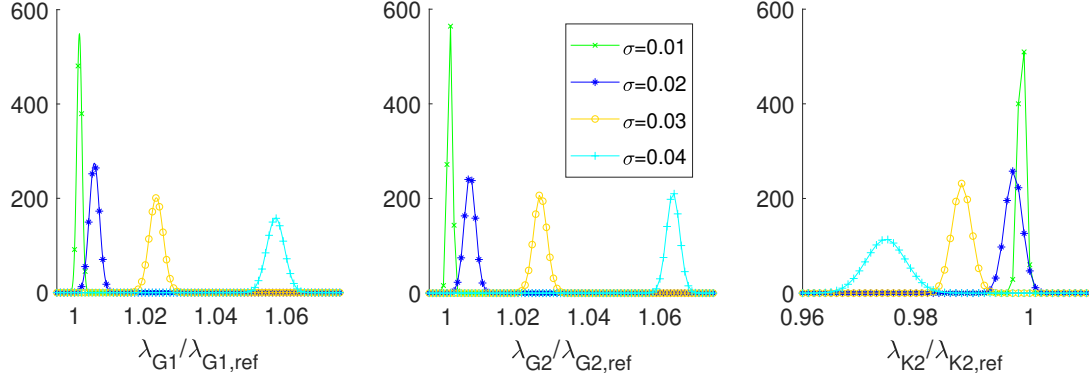


Figure 28: Approximated posterior PDFs of individual material parameters for the MHA sampling in Fig. 13.

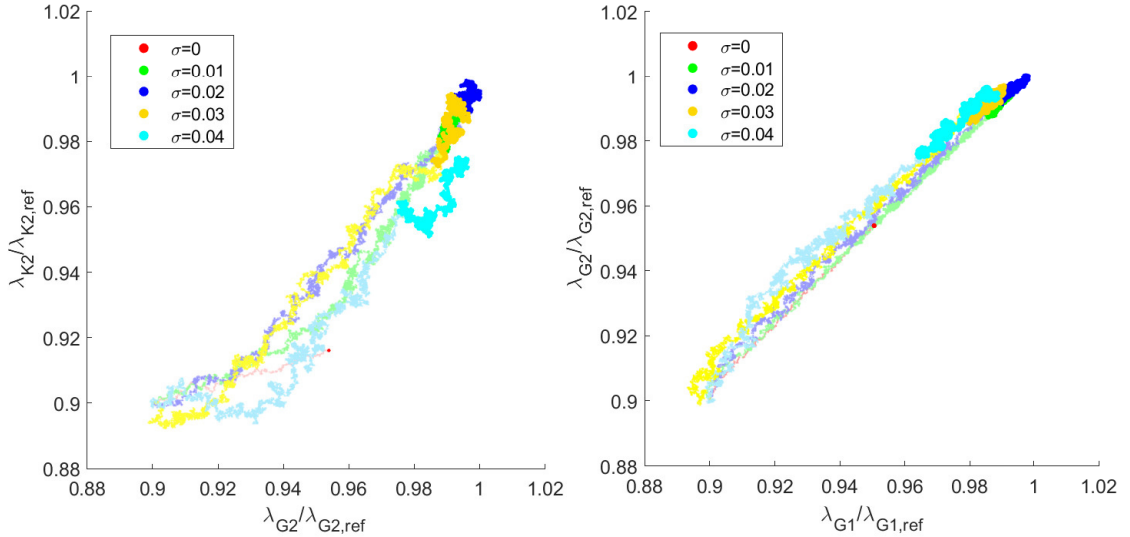


Figure 29: 2D projection of MHA sampling in material parameter dimensions, fibre shear modulus G_2 and bulk modulus K_2 (left), matrix shear modulus G_1 and fibre shear modulus G_2 (right); number of DOFs $t = 2 \times 61$ (25%), FE basis, single MC iteration, increasing $\sigma \in [0, 0.04]$, $N = 16\,000$ steps of MHA, starting point $0.9\lambda_{i,\text{mat}}$, tensile test.

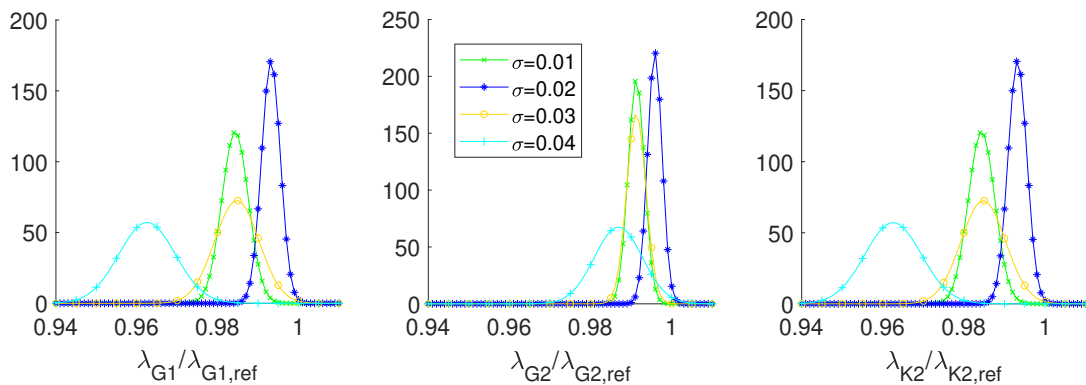


Figure 30: Approximated posterior PDFs of individual material parameters for the MHA sampling in Fig. 29.

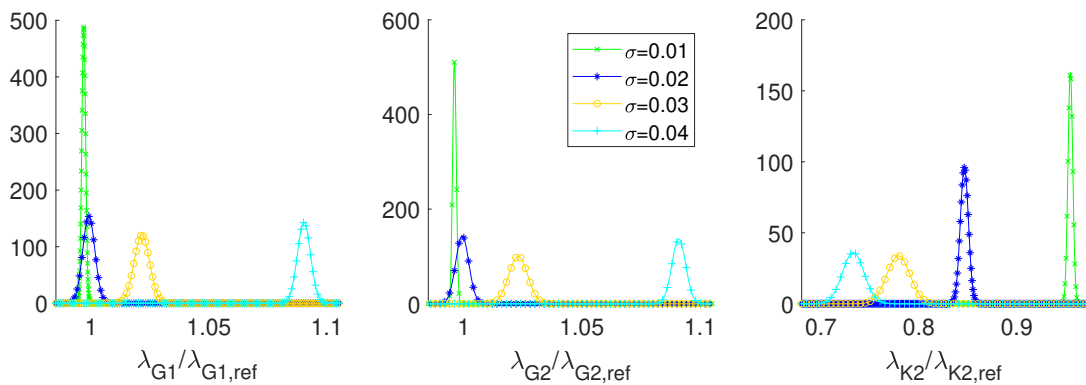


Figure 31: Approximated posterior PDFs of individual material parameters for the MHA sampling in Fig. 15.

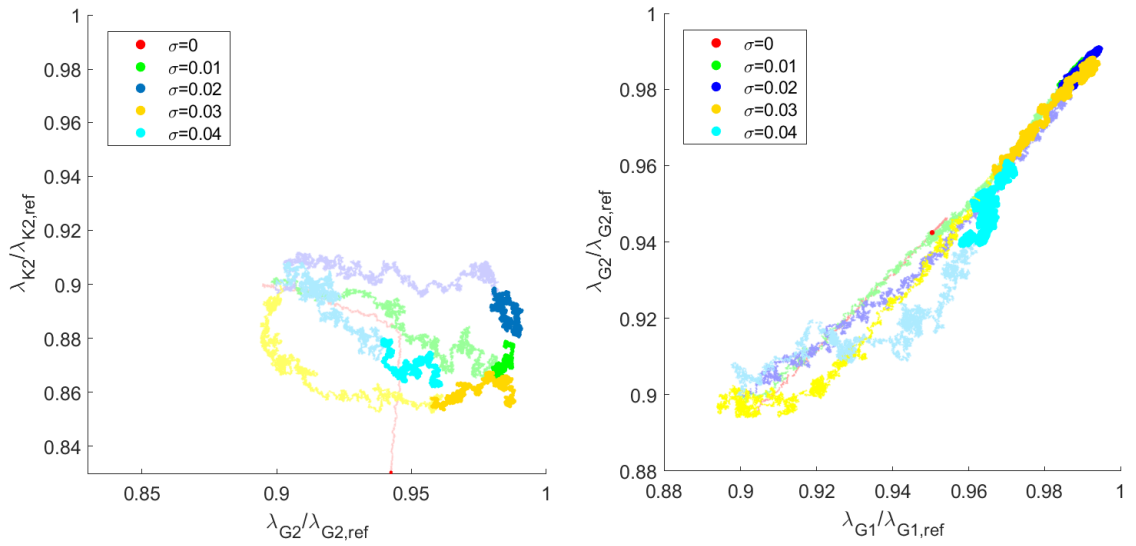


Figure 32: 2D projection of MHA sampling in material parameter dimensions, fibre shear modulus G_2 and bulk modulus K_2 (left), matrix shear modulus G_1 and fibre shear modulus G_2 (right); number of DOFs $t = 2 \times 61$ (25%), FE basis, single MC iteration, increasing $\sigma \in [0, 0.04]$, $N = 16\,000$ steps of MHA, starting point $0.9\lambda_{i,\text{mat}}$, shear test.

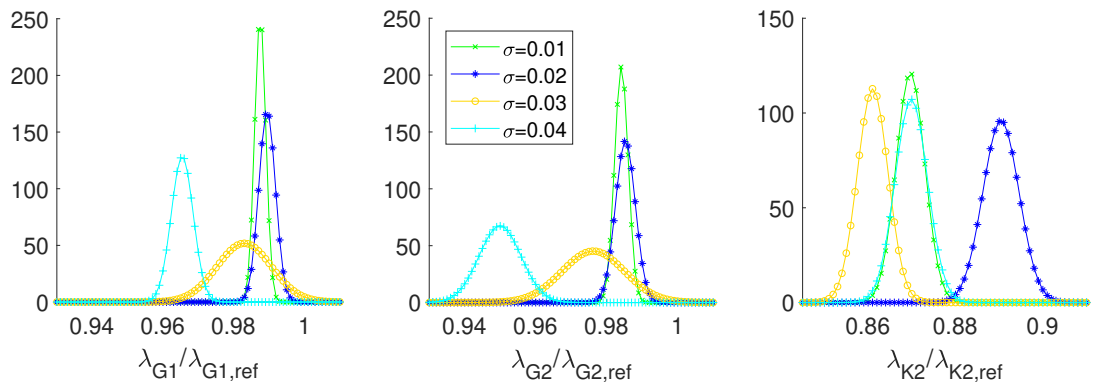


Figure 33: Approximated posterior PDFs of individual material parameters for the MHA sampling in Fig. 32.

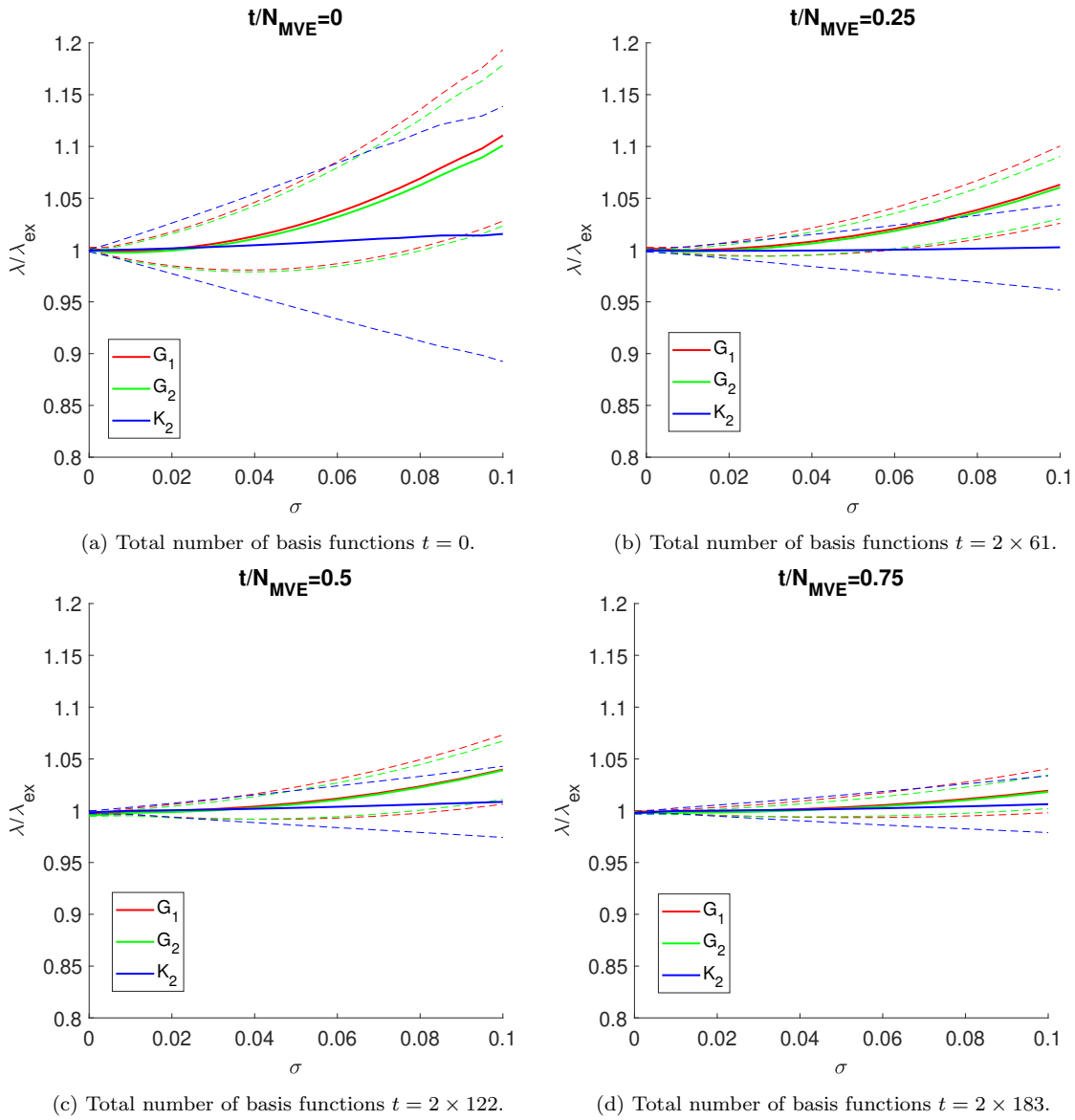


Figure 34: Identified parameters for the different number of KLE basis functions, mean (solid) \pm standard deviation (dashed), increasing $\sigma \in [0, 0.1]$, $N = 4\,000$ steps of MHA, KLE approximation of noise by least squares method is subtracted from the boundary conditions with noise, fixed boundary conditions, tensile test.

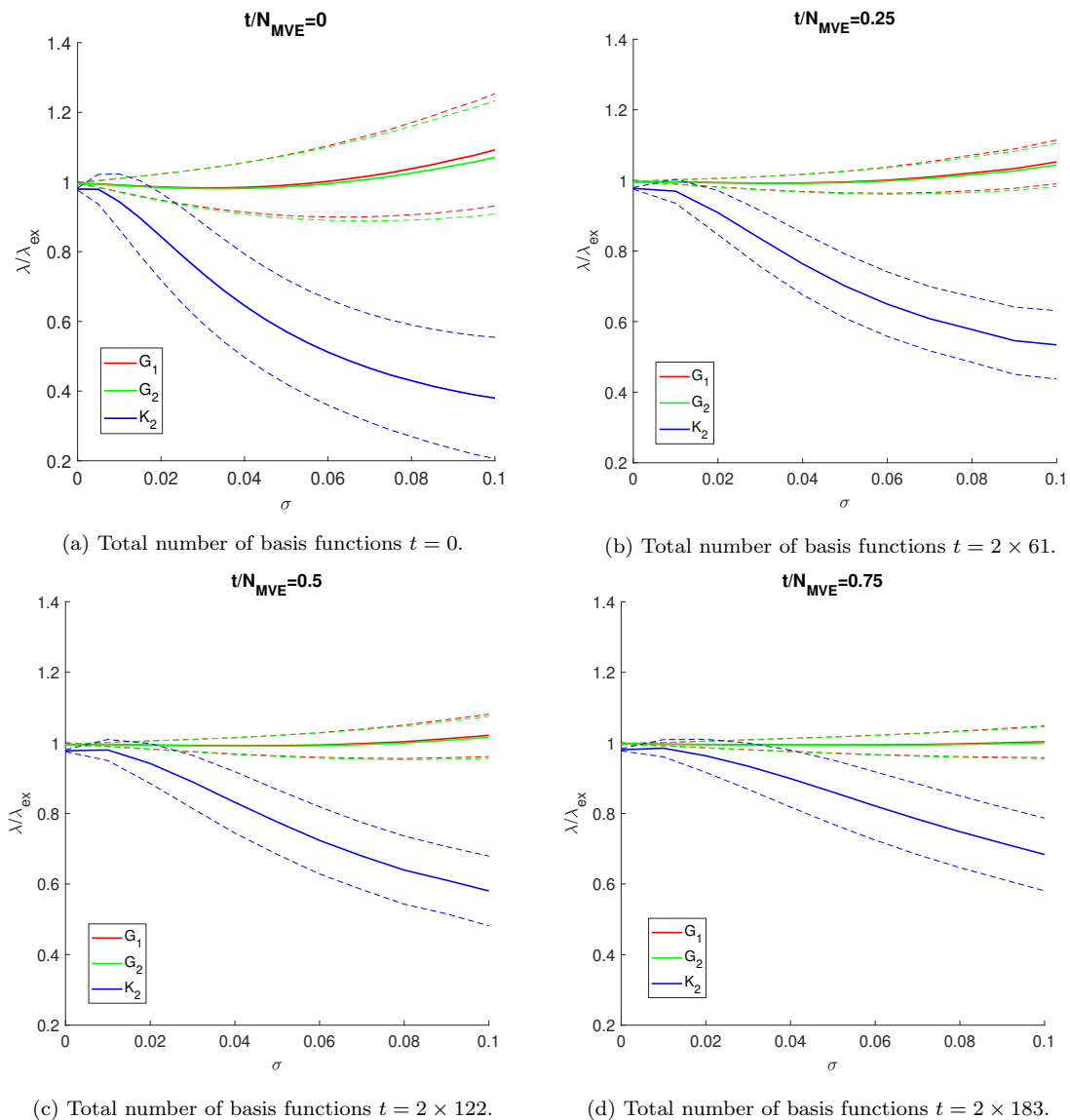


Figure 35: Identified parameters for the different number of KLE basis functions, mean (solid) \pm standard deviation (dashed), increasing $\sigma \in [0, 0.1]$, $N = 4\,000$ steps of MHA, KLE approximation of noise by least squares method is subtracted from the boundary conditions with noise, fixed boundary conditions, shear test.

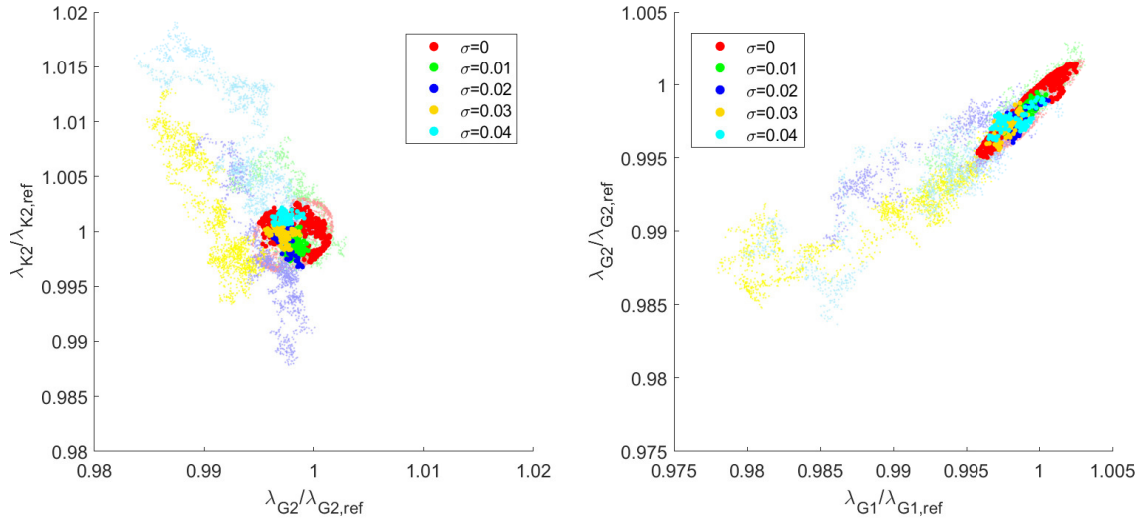


Figure 36: 2D projection of MHA sampling in material parameter dimensions, fibre shear modulus G_2 and bulk modulus K_2 (left), matrix shear modulus G_1 and fibre shear modulus G_2 (right); number of DOFs $t = 2 \times 244$ (100%), KLE basis, single MC iteration, increasing $\sigma \in [0, 0.04]$, $N = 16\,000$ steps of MHA, the starting point of MHA is the last accepted sample of each MC iteration for a given σ from the MHA with fixed boundary experiment in Section 5.2, tensile test.

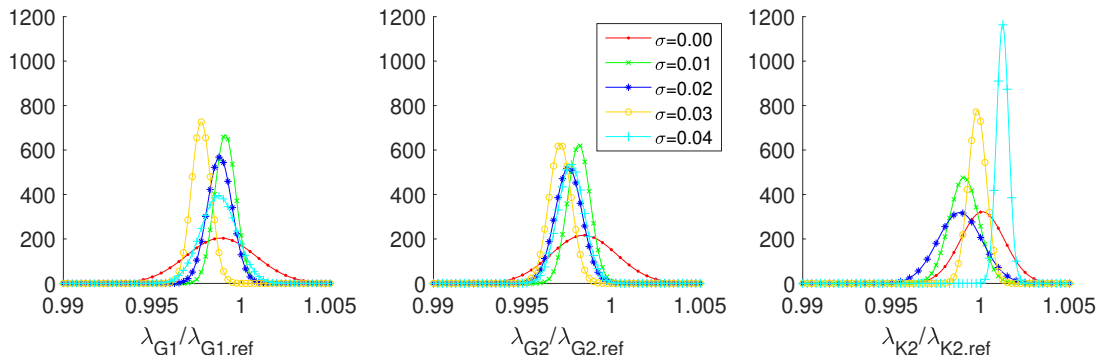


Figure 37: Approximated posterior PDFs of individual material parameters for the MHA sampling in Fig. 36.

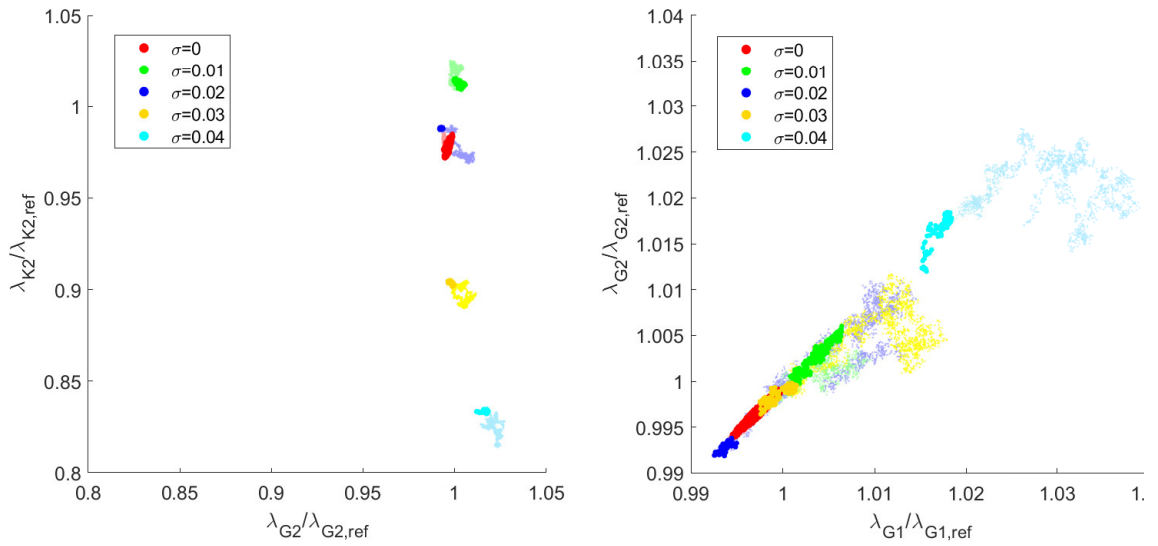


Figure 38: 2D projection of MHA sampling in material parameter dimensions, fibre shear modulus G_2 and bulk modulus K_2 (left), matrix shear modulus G_1 and fibre shear modulus G_2 (right); number of DOFs $t = 2 \times 244$ (100%), KLE basis, single MC iteration, increasing $\sigma \in [0, 0.04]$, $N = 16\,000$ steps of MHA, the starting point of MHA is the last accepted sample of each MC iteration for a given σ from the MHA with fixed boundary experiment in Section 5.2, shear test.

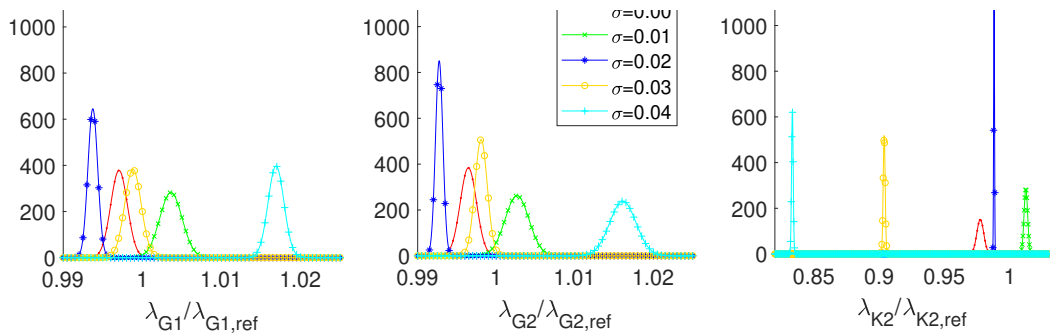


Figure 39: Approximated posterior PDFs of individual material parameters for the MHA sampling in Fig. 38.

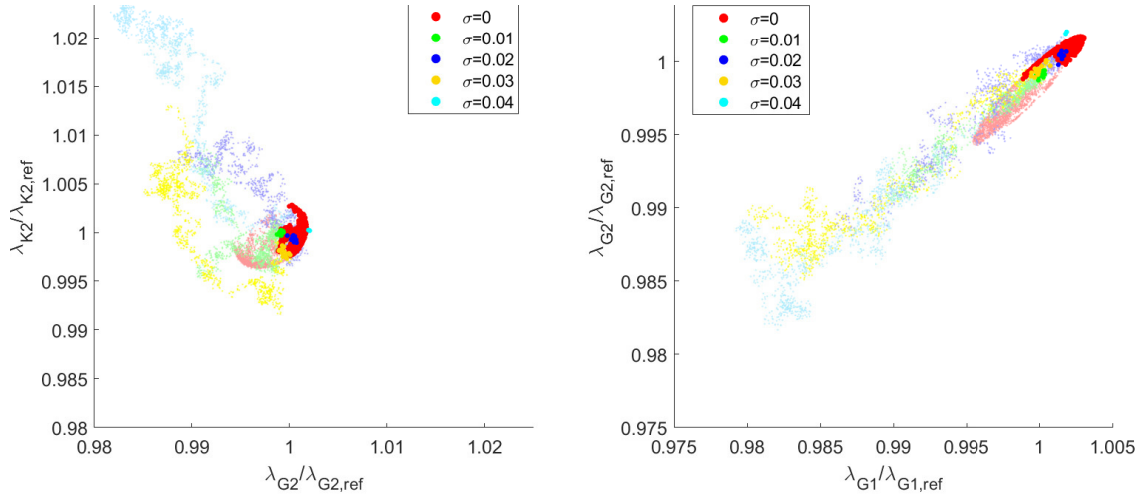


Figure 40: 2D projection of MHA sampling in material parameter dimensions, fibre shear modulus G_2 and bulk modulus K_2 (left), matrix shear modulus G_1 and fibre shear modulus G_2 (right); number of DOFs $t = 2 \times 61$ (25%), KLE basis, single MC iteration, increasing $\sigma \in [0, 0.04]$, $N = 16\,000$ steps of MHA, the starting point of MHA is the last accepted sample of each MC iteration for a given σ from the MHA with fixed boundary experiment in Section 5.2, tensile test.

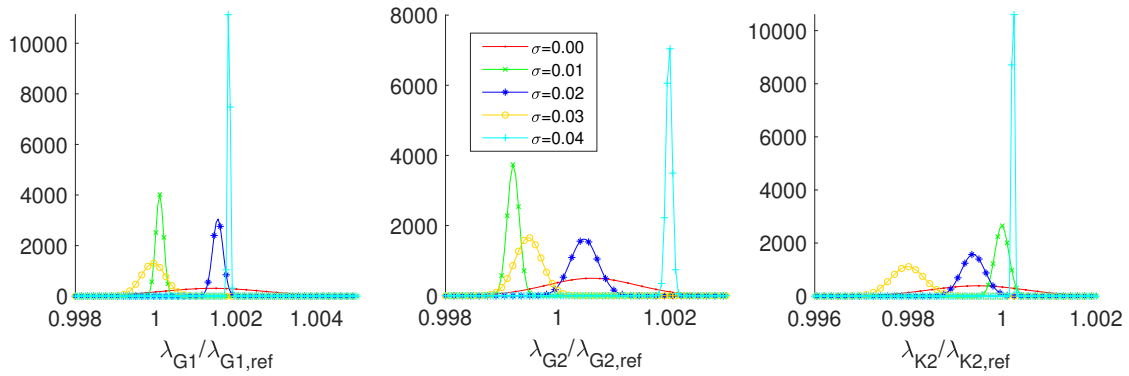


Figure 41: Approximated posterior PDFs of individual material parameters for the MHA sampling in Fig. 40.

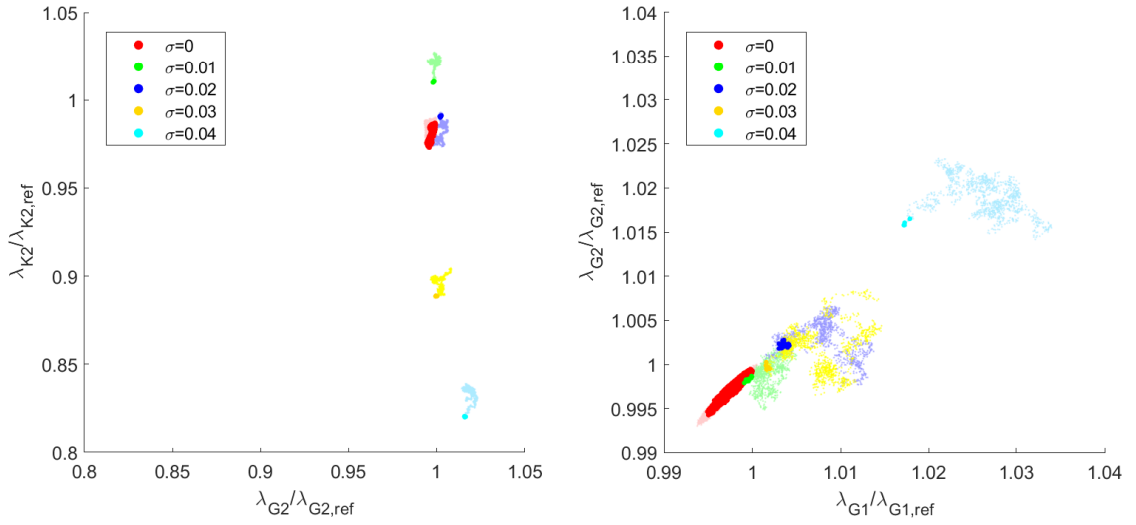


Figure 42: 2D projection of MHA sampling in material parameter dimensions, fibre shear modulus G_2 and bulk modulus K_2 (left), matrix shear modulus G_1 and fibre shear modulus G_2 (right); number of DOFs $t = 2 \times 61$ (25%), KLE basis, single MC iteration, increasing $\sigma \in [0, 0.04]$, $N = 16\,000$ steps of MHA, the starting point of MHA is the last accepted sample of each MC iteration for a given σ from the MHA with fixed boundary experiment in Section 5.2, shear test.

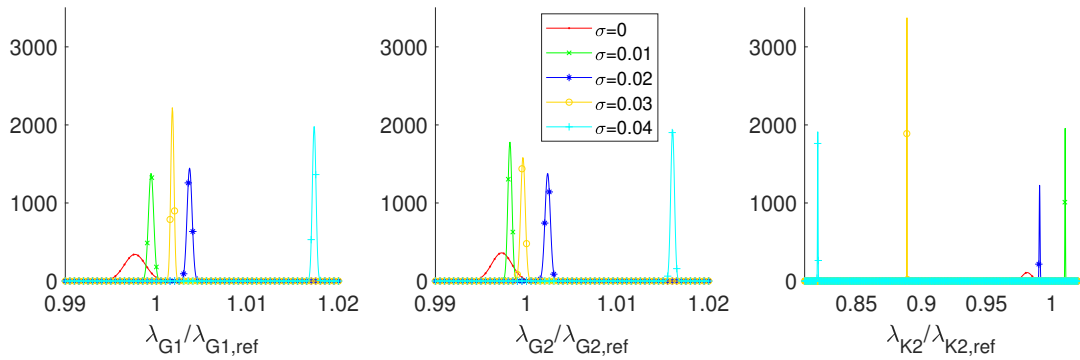


Figure 43: Approximated posterior PDFs of individual material parameters for the MHA sampling in Fig. 42.